

Petrology and Geochemistry of Ultramafic-Mafic Suite of Rocks from the Singhbhum Craton, Eastern India: Implications on Petrogenesis and Geodynamic Setting

Pawan Kumar Yadav¹, Manorama Das²

Geological Survey of India, SU: Bihar, Lohia Nagar, Kankarbagh, Patna – 800020, India

*Corresponding author. E-mail: [pawankumaryadavgsi\[at\]gmail.com](mailto:pawankumaryadavgsi[at]gmail.com)

Abstract: *This work intends to present a detailed field characteristic, petrographic, mineral chemistry, and whole-rock geochemical data of the ultramafic-mafic suite of rocks for the first time in Purnapani and Asanbani areas, Singhbhum Craton, India. It is a contribution to constrain the alteration processes, crustal contamination, tectono-magmatic evolution, geodynamic setting, and mantle composition of the ultramafic-mafic suite for the first time in the study area. A petrographic study shows that ultramafic rock is represented by the peridotite whereas the mafic rocks are identified as gabbro and anorthositic gabbro. The peridotite shows low SiO₂ (39.29-45.04 wt.%), Al₂O₃ (3.15-4.49 wt.%), and TiO₂ (0.25-0.47 wt.%) contents and high contents of MgO (27.41-35.25 wt.%), CaO (2.44-7.07 wt.%), LOI (4.05-8.32 wt.%), Ni (130-1700 ppm), Cr (425-8240 ppm), and V (123-260 ppm). It shows low variation in (La/Yb)_N = 1.20-3.90; (La/Sm)_N = 0.97-2.96; (Gd/Yb)_N = 0.75-1.29, (Sm/Nd)_N = 0.79-2.24 ratios, Σ REE (11.73-23.66 ppm), and positive Eu anomalies (Eu/Eu* = 1.96-8.69). Besides, gabbro and anorthositic gabbro exhibit relatively higher SiO₂ (50.28-53.84 wt.% in gabbro; 50.85-57.44 wt.% in anorthositic gabbro), Al₂O₃ (10.39-15.74 wt.%; 14.03-22.63 wt.%), and CaO (6.66-8.85 wt.%; 6.34-8.61 wt.%) contents and lower MgO (4.85-7.66 wt.%; 1.02-3.56 wt.%), and LOI (1.37-1.97 wt.%; 0.87-2.34 wt.%). Their rare earth and trace element patterns exhibit mild to moderate fractionation with coherent patterns (La/Yb = 4.43-9.65 in gabbro; 5.22-20.20 in anorthositic gabbro), Eu anomalies (Eu/Eu* = 0.64-1.22 in gabbro; 0.67-0.85 in anorthositic gabbro), and negative Nb anomalies. The analyzed data of the ultramafic-mafic suite were plotted in different discriminating diagrams for understanding the geodynamic setting. On the basis of the discriminating plots and the chemical characteristics, it can be stated that the derivation of ultramafic-mafic suites of rocks was generated through fractional crystallization of magma in a magma chamber at a transitional depth of the spinel-garnet regime with subsequent crustal contamination in a continental arc environment. The genesis of these ultramafic-mafic suites of rocks has quite coincided with the widespread crustal growth event in the Singhbhum Craton.*

Keywords: Ultramafic-mafic suites, Geochemistry, Petrogenesis, Tectono-magmatic evolution, Singhbhum Craton

1. Introduction

Ultramafic-mafic suite of rocks provide a window to understand the composition of mantle sources and pressure and temperature conditions of melting and also provide valuable information for unraveling the geological history of orogenic belts (Herzberg and Zhang, 1996; Falloon et al., 2008; Polat et al., 2011; Su et al., 2011; Yellappa et al., 2014; Talbi et al., 2020). These rocks are significant in the way that they are established hosts for many metallic deposits especially the Cu-Ni-Cr and Platinum Group of Minerals (PGM) and associated sulfide deposits throughout the world (Ma et al., 2016). The association of these rocks are generally small in size and are elliptical- to ring-shaped complexes with distinct zoned rock units, the peridotites in the core, whereas pyroxenites and gabbros-anorthositic gabbro occur at the outer parts of the intrusion. The convergent plate margins are a known place for the formation of this type of rock, besides it can also occur in almost any geodynamic setting (Irvine, 1974; Tistl, 1994; Himmelberg and Loney, 1995; Mues-Schumacher et al., 1996; Chai et al., 2008; Chen et al., 2009; Yang and Zhou, 2009). The Kaapvaal Craton and Bushveld Layered Igneous intrusion in South Africa, Emeishan Large Igneous Province of Southwest China, Zimbabwe Craton, and the Singhbhum and Dharwar cratons of the Indian shield were the established worldwide cratons to host the Cu-Ni-Cr, PGM,

and associated sulfide deposits in the ultramafic-mafic suite (DeWit and Tredoux, 1987; Mondal et al., 2001, 2008; Naldrett et al., 2008; Prendergast, 2008; Zhu et al., 2010; Mukherjee et al., 2010, 2012; Khatun et al., 2014; Ma et al., 2016; Manikyamba et al., 2020).

In the Indian subcontinent, ultramafic-mafic intrusive complexes consisting of intrusive dunite, peridotite, pyroxenite, gabbro, and anorthosite associated with extrusive komatiite and pillowed basalts are reported from Paleoproterozoic and Mesoproterozoic greenstone belts (Mondal et al., 2001, 2008; Jayananda et al., 2008; Mukherjee et al., 2010, 2012; Khatun et al., 2014; Ramiz et al., 2018; Manikyamba et al., 2020). In the Singhbhum Craton, several major granitic batholiths that are associated with volcano-sedimentary sequences, as well as gabbro anorthositic bodies with or without sharp contacts, are noticed by several workers (Saha, 1994; Misra, 2006; Nelson et al., 2014; Mitra et al., 2019; Olierook et al., 2019; Manikyamba et al., 2020). The comprehensive works on the genesis of PGE, silver, chromite, and Ni-Cu mineralization in the ultramafic-mafic suite in Nuasahi and Sukinda areas were mostly carried out (Mondal et al., 2001, 2006; Mondal, 2009; Khatun et al., 2014; Bhattacharjee and Mondal, 2021). In addition, geological, geochronological, and geochemical investigations of the gabbro-anorthosite complex from Singhbhum Craton for understanding their petrogenesis, age of emplacement, tectono-magmatic evolution, relationship

Volume 11 Issue 12, December 2022

www.ijsr.net

Licensed Under Creative Commons Attribution CC BY

with the granitoid magmatism, and crustal growth were attempted (Chakroborti et al., 2019b; Manikyamba et al., 2020). Based on the available information, the combined works on the petrogenesis and tectonic setting of the ultramafic-mafic suite (gabbro-anorthosite) of rocks are yet to be established in the Singhbhum Craton.

In this paper, we present a detailed field characteristic, petrographic, mineral chemistry, and whole-rock geochemical data of the ultramafic-mafic suite of rocks (peridotite-gabbro and anorthositic gabbro) for the first time in Purnapani and Asanbani areas, Mayurbhanj district of Odisha, Singhbhum Craton, Eastern India. Besides, the effort has also been made to recognize the post-magmatic alteration processes, crustal contamination, petrogenesis, tectono-magmatic evolution, geodynamic setting, and composition of the mantle source.

2. Regional Geological Setting

The Singhbhum Craton (SC) is a polycyclic Archaean crustal block of Palaeo-Mesoarchean age which is bounded by a tectonic framework of the Baster cratonic block in the west, gigantic area of alluvium to the east, the Eastern Ghats Mobile Belt (EGMB) in the south, and the Chottanagpur Gneissic Complex (CGC) in the north (Fig. 1; Saha, 1994). The eastern part of SC preserves the records of multiple episodes of volcanism, sedimentation, and metallogenic events spanning from Paleoproterozoic to Mesoproterozoic (Saha, 1994; Misra, 2006; Nelson et al., 2014; Mitra et al., 2019; Pandey et al., 2019; Chakroborti et al., 2019a). The Older Metamorphic Group (OMG) of rocks is dated in ~3.5 - 3.6 Ga which are represented by the pelitic schist, arenite, para, and ortho- amphibolites (Saha, 1994; Misra et al., 1999; Mukhopadhyay, 2001; Misra, 2006). Rocks of the OMG are laterally intruded by the Older Metamorphic Tonalite Gneiss (OMTG) which represents the first stable continental crust, is dated around 3.44 Ga (Goswami et al., 1995; Acharyya et al., 2010a). Later on, the OMG and OMTG are intruded by the younger phases of Singhbhum Granitoid which consists of five distinct plutons emplaced around 3.3 Ga (Misra et al., 1999). Besides, the new-age data on the various phases of the Singhbhum Granitoids were presented by several workers (Tait et al., 2011; Upadhyay et al., 2014; Nelson et al., 2014). The sedimentation in the SC began with the deposition of the Iron Ore Group (IOG) rocks which are represented by low-grade volcano-sedimentary successions comprising meta-volcanics, felsic and intermediate volcanics, ultramafics, spinifex textured peridotitic komatiite, quartz-pebble conglomerate, quartzites, banded iron formation, metachert with minor carbonate rocks (Yadav et al., 2015, 2016; Chaudhuri et al., 2015, 2017; Yadav and Das, 2017a, c, d, 2019a, 2020a, b). The three major Archean greenstone belts hosting the IOG are the Badampahar-Gorumahisani greenstone belt or the eastern IOG; the Tomka-Daitari greenstone belt or the southern IOG, and the Noamundi-Jamda-Koira greenstone belt or the western IOG (Mondal, 2009; Manikyamba et al., 2020; Table 1).

Several ultramafic-mafic bodies including peridotite, pyroxenite and gabbro-anorthosite suit occur along the Badampahar-Gorumahisani greenstone belt to Nuasahi

region at the eastern margin of the Singhbhum Craton (Saha, 1994; Roy and Bhattacharya, 2012; Pradhan et al., 2012; Manikyamba et al., 2020). Dunn and Dey (1942) considered the gabbro-anorthosite bodies occurring along the eastern margin of the Singhbhum Granite batholith to be of pre-Singhbhum Granite age and they grouped it under basic rocks associated with the 'Iron Ore Stage'. Chatterjee (1945) working on the gabbroid rocks of the Gorumahisani region was first to demonstrate that these gabbroid rocks are intrusive into the Singhbhum granite, but he considered the gabbro to be younger than the granophyric granite lying to the east. Later on, Sarkar and Saha (1962, 1963) considered the gabbroid bodies to be post-Singhbhum Granite and considered it as an early comagmatic phase of the granophyre. Afterward, Saha et al. (1977) argued that the gabbro-anorthosite suit and the granophyre are not comagmatic and the former is distinctly older than the granophyre. Mishra et al. (1999) suggested that the gabbroid bodies and granophyre of Mayurbhanj were possibly comagmatic. The different phases of the Singhbhum granitoids range in age from 3.44-3.12 Ga (SBG-I = 3.44 Ga; SBG-II = 3.3 Ga and SBG-III = 3.12 Ga; Mishra et al., 1999; Table 1). The ultramafic-mafic bodies are small-scale intrusions exposed along the contact zones of Dhanjori, and IOG in the north, and at the contact of IOG, Mayurbhanj, and Besoi granite in the northeast. These bodies show the intrusive relationship with the in the Singhbhum granite phase - III (SBG-III), Mayurbhanj Granite (MBG), and the Kaptipada granitic pluton (Fig. 1; Saha, 1994; Pradhan et al., 2012; Manikyamba et al., 2020; Table 1). Besides, the Sukinda and Baula-Nuasahi mineralized gabbro-anorthosites and layered ultramafic complexes have separated as a different entity.

3. Geology of the study area

The studied area exposes the rocks types belonging to OMTG, Badampahar Group, Singhbhum Granitoids, the mafic-ultramafic suite of rocks, and swarms of dyke of dolerite (Pradhan et al., 2012; Fig. 2). The Badampahar Group of rocks are represented by meta-andesite. The Singhbhum Granitoids are represented by tonalite-granodiorite gneiss of OMTG and equigranular granodiorite-monzogranite of the Singhbhum Granite Phase-B (SBG-B). The tonalite-granodiorite gneiss forms the basement for the Badampahar Group of rocks whereas the equigranular granodiorite-monzogranite of the SBG-B is intrusive into the Badampahar Group (Fig. 2). The tonalite-granodiorite gneiss occurs as xenolith within the granodiorite-monzogranite which is observed to the north of Mitwani (Fig. 2). It is leucocratic to mesocratic, medium to coarse-grained, foliated, and consists of quartz, plagioclase, K-feldspar as dominant minerals. The accessory minerals are represented by hornblende, biotite, epidote, and opaque. The gneissosity is defined by alternate bands of felsic and mafic minerals having variable thickness from few mm to cm. Two bands of meta-andesite are exposed on either side of Purnapani village having a discontinuous strike length of about 3 km with a width varying between 20 to 50m. Its trend swings from NNW-SSE to NNE-SSW. It is leucocratic, fine to medium-grained, foliated, and highly deformed rock which consists of alternate layers of altered plagioclase and pyroxene as essential minerals. On the weathered surface,

some elongated voids are arranged regularly. The study area is predominantly occupied by the equigranular granodiorite-monzogranite which mostly occurs in the plain area. It is leucocratic, massive, coarse to medium-grained rock and comprises quartz (white and smoky quartz), plagioclase, and K-feldspar as major minerals with hornblende and epidote as accessories. Syenogranite belonging to the Mayurbhanj Granite is exposed in the southeast of Purnapani (Fig. 2). It is leucocratic, medium-grained feebly deformed, and consists of quartz, alkali feldspar, and plagioclase as essential minerals. Besides, the swarms of basic dykes comprising mostly of doleritic composition are also mapped in the study area. It is mesocratic to melanocratic, medium-grained with plagioclase and pyroxene as major minerals constituents, and exhibits sub-ophitic texture. Specks of sulphide minerals like pyrite and chalcopyrite are observed a few places.

Ultramafic bodies are observed in and around Purnapani which shows an intrusive relationship with the meta-andesite and SBG-B. Three separate ultramafic bodies are delineated in the study area. The first body is exposed southwest of Churkasahi which occurs as a small mound within the SBG-B. The length and width of this body are approximately 1 km x 500 m trending NNE-SSW. The second ultramafic unit is exposed northwest of Purnapani occurring as a linear body trending N30°W-S30°E over a strike length of 500 m with a width of 70 m. The largest of the ultramafic bodies is exposed between the southeast of Purnapani and north of Asanbani occupying both plain areas and hilly terrain. It is surrounded by granodiorite (SBG-B) in the west, medium-grained syenogranite (Mayurbhanj Granite) in the north, and anorthositic gabbro in the southeast. It is mesocratic to melanocratic, medium-grained, highly foliated (Fig. 3a & b), and composed dominantly of mafic minerals like olivine, pyroxene, and amphibole. Towards the periphery, the rock is fine to medium-grained and highly foliated, and in the central part, it is coarse to very-grained and less foliated (Fig. 3c). Based on petrographic studies, it is represented by the peridotite (Fig. 3a to c).

The gabbro-anorthositic gabbro suite shows the intrusive relationship with the SBG-B and is exposed as linear and discontinuous bodies to the south of Purnapani and east of Asanbani (Fig. 2). The gabbroic rocks are mesocratic, grayish-green, massive, bouldery nature in outcrop and comprises of plagioclase and pyroxene as major minerals along with quartz, ilmenite, magnetite, and epidote as accessories (Fig. 3d). The gabbros exhibit a wide variation in the proportion of pyroxene and plagioclase in hand specimen. The weathered surface of the gabbro is usually rough, hackly, with magnetite and pyroxene crystals projecting outward as the lath-shaped plagioclases occupying the hollows. The encrustation of vanadiferous-titanium- magnetite was observed in the central part of the gabbro body, south of Purnapani (Fig. 3e). The anorthositic gabbro is bordered by the ultramafic rock on the northern side and SBG-B on the western side which is mostly exposed in the plain area. Megascopically, it is leucocratic, coarse to very coarse-grained, at place pegmatoidal in nature, massive, hard, undeformed, and mainly composed of lath of plagioclase and stubby grains of pyroxenes (Fig. 3f & g). East of Asanbani, the evidence of mingling between the

anorthositic gabbro and syenogranite of the Mayurbhanj Granite is also noticed within this unit (Fig. 3h).

4. Petrography of ultramafic-mafic suite of rocks

Based on the petrographic study, ultramafic is identified as peridotite which is fine to medium-grained, commonly exhibiting cumulate and intercumulate textures, and mainly consists of olivine, serpentine, enstatite, (Fig. 4a) hypersthene, diopside, and augite. Accessories are represented by hornblende, plagioclase, and secondary magnetite. The primary minerals like olivine and pyroxenes are mostly replaced by secondary minerals viz. serpentine, magnetite, chlorite, talc, and tremolite. Mesh texture formed due to the breakdown of olivine into serpentine and secondary magnetite which is corroborated by the BSE image (Fig. 4a & b). At places, grain size variations from medium to coarse-grained are also noticed within this rock (Fig. 4c). Based on the modal analysis, the peridotite modally together constitutes 50% olivine, 29% clinopyroxene, and 21% orthopyroxene and falls in the lehrzolit field.

On the basis of mineral proportion and modal mineralogy, the mafic suit of the study area is classified as gabbro and anorthositic gabbro. Gabbro is medium to coarse-grained, comprising plagioclase, augite, and hypersthene as essential minerals with a lesser amount of quartz, apatite, actinolite-tremolite, chlorite, epidote, zoisite, and magnetite. The rock shows ophitic, sub-ophitic, hypidiomorphic, and myrmekite textures. The ophitic and sub-ophitic textures are defined by the early formed cumulus phase of plagioclase crystals that are fully or partially enveloped by the pyroxene crystals (Fig. 4d). The presence of clinopyroxene, orthopyroxene, and plagioclase imply a common magma parentage (Fig. 4d & e). At places, pyroxene is partially replaced by hornblende, and plagioclase is altered to epidote and zoisite. In most places, crystals of pyroxenes occur as individuals but at places, intergrowth crystals are also observed. In the intergrowths of clinopyroxene (augite) and orthopyroxene (enstatite), enstatite occurs as blebs or lamellae within the augite or called as inverted pigeonite (Fig. 4e & f). These intergrowths of pyroxene have been formed due to the inversion of pigeonite to orthopyroxene in exsolution with augite. In modal analysis, it contains 55% plagioclase, 40% clinopyroxene, and 5% orthopyroxene and it plots in the gabbro field. Petrographic study reveals that the anorthositic gabbro is coarse to very coarse-grained rock having ophitic, sub-ophitic, hypidiomorphic, and myrmekite textures. It is composed of large euhedral grains of plagioclase and augite as essential minerals and quartz, magnetite, hornblende, and sericite as accessories (Fig. 4g & h). The alteration of augite into hornblende is also noticed in a few places (Fig. 4g). The plagioclase grains are fractured and developed myrmekitic intergrowth with quartz indicating thermal perturbations during their cooling stage. The plagioclase crystals show euhedral habit with bent lamellar twinning, indicating the deformation signatures (Fig. 4h). In modal analysis, it has 80% plagioclase, 18% clinopyroxene, and 2% orthopyroxene and falls in the anorthositic gabbro field.

5. Analytical techniques

The Electron Probe Microanalyses (EPMA) of selected samples from the peridotite, gabbro, and anorthositic gabbro (TK-139, TK-93, TK-86) were carried out at EPMA Laboratory, Geological Survey of India (GSI), Southern Region, Hyderabad, India, using CAMECA Sx100 instrument. Compositions of olivine, clinopyroxene, orthopyroxene, amphibole, and plagioclase were measured with an accelerating voltage of 15 kV, beam current 20 nA, beam diameter 1 μ m, and a counting time of the 20s on peaks and 10s on the background. All the natural silicates except Mn and Ti and synthetic oxides were used as standards for all element analysis. The analytical compositions of minerals of the different studied rocks are provided in tables 2 to 4.

Twenty-one representative samples of the ultramafic-mafic suite were collected from the fresh outcrops; namely, peridotite (8 nos.), gabbro (8 nos.), and anorthosite (5 nos.) representing the Intrusive unit belonging to the Archean (Fig. 2). Due care has been taken in selecting the least altered samples for chemical analysis after the detailed petrographic examination. All the samples were sent for the analysis of major oxides, trace elements, and REE by X-Ray Fluorescence (XRF) and Inductively Coupled Plasma Mass Spectrometer (ICPMS) instruments respectively at Chemical Laboratory, Geological Survey of India, Eastern Region, Kolkata, India. During the sample preparation process, the outer or weathered portions of all the samples were removed to minimize alteration problems. The samples were well pulverized to minus 200 mesh size using a planetary ball mill (Restch PM400) in agate bowl and balls and about five hundred grams of sample was collected. For Chemical analysis of rock samples using the XRF technique, the pulverized samples were pressed in the form of a pressed pellet of 40 mm diameter in an aluminum cup over a bed of boric acid by applying a pressure of 20 tonnes in a Hydraulic press pelletizer (Insmart Systems). The prepared pellets were analyzed in a 2.4kW WD sequential X-ray fluorescence spectrometer (PAN analytical Magix - 2424) having PX1, PE 002, Ge 111, LiF 200, LiF 220 diffracting crystals and flow scintillation and duplex detectors. For the chemical analysis of the sample by ICPMS technique, 0.1 gram pulverized sample of minus 200 mesh size was made to dissolve in 1:2 ratios of hydrofluoric acid and perchloric acid (3 ml and 6 ml respectively) in a Teflon beaker. The mixture was kept overnight for cold digestion after that it was placed over a hot plate at 220°C for hot digestion in a closed system. When the hydrofluoric acid has been removed completely, the remaining mixture was evaporated to a yellowish pasty mass. The pasty mass was dissolved in 50 ml of 8-10% nitric acid. The solution was transferred to a volumetric flask and made up of a 250 ml clear homogeneous solution. In this solution, 5 ml of 500 ppb indium nitrate solution was added as internal standard. The final solution was quantitatively analyzed by ICPMS (Thermo Fischer CAP-Q). Analytical precision and accuracy of data obtained at these laboratories are comparable with the international reference standards. Both laboratories i.e. XRF and ICPMS have National Accreditation Board for Testing and Calibration Laboratories (NABL) accreditation ISO/IEC 17025:2017 (Certificate No.: TC-5956) and analytical work for the samples had been carried out in

compliance with NABL guidelines. The analytical data are presented in table 5 and 6.

6. Mineral Chemistry

6.1 Olivine: Olivine occurs as a cumulus phase in peridotite which shows the magnesian composition (X_{Mg}) ranges from 0.74 to 0.86 and ferrous composition (X_{Fe}) vary in the ranges from 0.14 to 0.26. The Cr_2O_3 content in olivine varies from 0.009 to 0.077 (Table 2). The chemical composition of olivine falls in the chrysolite field while plotted in a binary diagram (Fig. 5a).

6.2 Pyroxene: Diopside and clinoenstatite are the main pyroxenes depicted in the peridotite which are showing compositional range of $Wo_{1.7-47.5}En_{42.2-70.1}Fs_{9.7-28.5}$, with CaO (0.86-25.67 wt.%); Na_2O (0.005-0.22 wt.%); Al_2O_3 (0.94-1.50 wt.%); Cr_2O_3 (0.07-0.19 wt.%), and TiO_2 (0.01-0.11 wt.%). Pyroxene compositions when plotted in the Wo - En - Fs diagram (Morimoto et al., 1988) mostly fall in diopside and clinoenstatite fields (Fig. 5b). The mineral chemistry of pyroxene is given in table 2 with their structural formula and chemical compositions. Pyroxenes of the gabbro have mainly occupied the fields of augite, pigeonite, and clinoferrrosilite as plotted in the Wo - En - Fs diagram (Fig. 5b; Morimoto et al., 1988). Pyroxenes display the compositional range of $Wo_{2.22-44.50}En_{31.39-43.36}Fs_{23.79-54.74}$, with CaO (1-21.17 wt.%); Na_2O (0.01-0.29 wt.%); Al_2O_3 (0.27-1.51 wt.%); Cr_2O_3 (0.001-0.05 wt.%), and TiO_2 (0.12-0.36 wt.%). The analytical data of pyroxenes from gabbro are presented in table 3. The mineral chemistry of pyroxenes from anorthositic gabbro is displaying a compositional range of $Wo_{17.52-48.95}En_{19.30-28.39}Fs_{31.73-57.07}$. Their Al_2O_3 contents are ranging from 0.11 to 1.46 wt.%, whereas the CaO and Na_2O exhibit from 9.29 to 23.04 wt.% and 0.05 to 0.15 wt.% respectively (Table 4). The pyroxenes fall in the fields of hedenbergite, augite, and pigeonite (Fig. 5b).

6.3 Amphibole: Amphibole compositions of peridotite are plotted in $Mg/Mg+Fe+2$ vs. TSi diagram after Leake et al. (1997), the samples fall in edenite hornblende and pargasite hornblende fields (Fig. 5c). The analytical data of pyroxene is given in table 2 with their structural formula and chemical compositions. Analysed samples of anorthositic gabbro have mostly occupied the field of Fe-edenite hornblende (Fig. 5c), while plotted in binary diagram after Leake et al. (1997). The mineral chemistry data are presented in table 4.

6.4 Feldspar: Plagioclase from gabbro is lath and subhedral in nature and showing a bimodal size variation with pyroxene grains. The plagioclase grains show a compositional range of $An_{48.5}-An_{53.5}$ and predominantly plot in the field of labradorite except for one sample which falls in the andesine field (Fig. 5d). They show a moderate range of CaO (10.30-12.94 wt.%), Na_2O (4.99-5.67 wt.%), K_2O (0.30-0.37 wt.%), and Al_2O_3 (26.37-27.26 wt.%). The analytical data are given in table 3. The mineral chemistry of plagioclase from anorthositic gabbro shows a low concentration of $An_{2.7}-An_{43.1}$ and mainly falls in the field of andesine except two, which occupy the field of albite (Fig. 5d). They show low to moderate CaO (0.54-11.11 wt.%), high Na_2O (6.24-13.45 wt.%), K_2O (0.07-0.59 wt.%), and Al_2O_3 (20.38-25.87 wt.%; Table 4).

7. Results and Discussion

7.1 Geochemical characteristic and classification of ultramafic-mafic suite

The major oxide concentrations of peridotite show SiO₂ contents ranging from 39.29 to 45.05 wt.%, depleted in Al₂O₃ (3.15-4.49 wt.%), enriched in MgO (27.41-35.25 wt.%), CaO (2.44-7.07 wt.%), low TiO₂ contents (0.25-0.47 wt.%), and high LOI (4.05-8.32 wt.%). The analytical results of trace elements show some noteworthy values viz., Cu (10-256 ppm), Ni (130-1700 ppm), Co (45-100 ppm), Cr (425-8240 ppm), V (123-260 ppm), and Zr (20-75 ppm). All the analyzed samples of peridotite show variation in Σ REE contents which varies from 11.73 to 23.66 ppm. The analytical data of peridotite are presented in table 5 and 6. Inversely, gabbro exhibits relatively higher SiO₂ and Al₂O₃ contents (50.28 to 53.84 wt.% and 10.39 to 15.74 wt.% respectively) and also shows lower MgO and LOI contents vary from 4.85 to 7.66 wt.% and 1.37 to 1.97 wt.% respectively. As far as the trace elements are concerned, the gabbro show higher concentration of mantle compatible elements (Cu= 55-410 ppm; Ni= 75-185 ppm; Co= 48-65 ppm; Cr= 15-215 ppm; V= 169-325ppm; Zr= 45-200 ppm; Σ REE= 45.88-188.95ppm; Table 6). Anorthositic gabbro samples show moderate SiO₂ contents that vary from 50.85 to 57.44 wt.%, high Al₂O₃ vary from 14.03 to 22.63 wt.%, and low MgO varies from 1.02 to 3.56 wt.% whereas the contents of CaO, TiO₂, and LOI vary from 6.34 to 8.61 wt.%, 0.28 to 1.60 wt.%, and 0.87 to 2.34 wt.% (Table 6). The trace elements values of anorthositic gabbro are Cu (15-330 ppm), Ni (15-55 ppm), Co (5-55 ppm), Cr (15-70 ppm), V (20-380 ppm), Zr (35-250 ppm), and Σ REE (51.52-111.88 ppm).

The analyzed samples of peridotite are plotted in the Al₂O₃-Fe₂O₃+TiO₂-MgO cationic ternary diagram fall in the komatiite field (Fig. 6a; Jenson, 1976). However, there is a peculiar spinifex texture is the absence in ultramafic samples so that, we avoided calling these rocks komatiites. Samples of mafic rocks including gabbro and anorthositic gabbro predominantly occupy the field of high-Fe tholeiite basalt and tholeiitic series except for one sample of anorthositic gabbro falls in calc-alkaline series (Fig. 6a). Mafic rocks occupy the field of gabbro (Fig. 6b) when plotted in the binary plot of Na₂O+K₂O vs. SiO₂ (Cox et al., 1979). Nb/Y vs. SiO₂ binary diagram in which the studied samples of gabbro and anorthositic gabbro falls in the field of subalkaline basalt and andesite (Fig. 6c; Winchester and Floyd, 1977). In the ternary plot of TiO₂*100+Y +Zr-Cr after Davies et al. (1979), all the samples of peridotite show enrichment of magnesium (Fig. 6d) whereas, the mafic suit depicts the tholeiitic to the calc-alkaline character (Fig. 6d).

7.2 Alteration and element mobility

Most of the Archean rocks which have undergone metamorphism and multiple phases of deformational events suffer a change in original geochemical signatures as well as textures. The petrographic study reveals peridotite is exhibiting cumulate and intercumulate textures and mainly consists of olivine, serpentine, hypersthene, enstatite, diopside, and augite. Olivine and pyroxenes are mostly

replaced by secondary minerals viz. serpentine, magnetite, chlorite, talc, and tremolite. The mafic suit is represented by gabbro and anorthositic gabbro. Gabbro is medium to coarse-grained, comprising plagioclase, augite, and hypersthene as essential minerals with a lesser amount of quartz, apatite, actinolite-tremolite, chlorite, epidote, zoisite, and magnetite. Anorthositic gabbro is coarse to very coarse-grained rock and is composed of large euhedral grains of plagioclase and augite as essential minerals and quartz, magnetite, hornblende, and sericite as accessories. The alteration of augite into hornblende is also noticed in a few places. Thus, the petrogenetic studies of ultramafic-mafic rocks require elements that are not much affected by post-magmatic alteration. The absolute concentration and their ratios can be used as effective geochemical proxies to evaluate mantle processes and source characteristics (Song et al., 2006).

Mobility of the major and trace elements during post magmatic alteration events is a major problem for the ultramafic-mafic rocks which have experienced multiple tectonothermal events (Ramiz et al., 2018). Mobility of LILE and REE is controlled by secondary processes such as induced hydrothermal alteration/element mobility and metamorphism in most Archean rocks across the world (Chavagnac, 2004; Yadav and Das, 2020b). In the study area, mobility of major oxides and trace elements like SiO₂, CaO, Al₂O₃, K₂O, Na₂O, and P₂O₅, TiO₂, and, LOI, Ba, Rb, Sr, Co, Cr, Ni, V, and Zr are noticed in the ultramafic-mafic suite (Fig. 7 & 8). In the binary variation diagrams of major elements oxides, low negative correlation has been observed in MgO versus SiO₂, Al₂O₃, Na₂O, CaO, and K₂O whereas the plot of LOI shows a slightly positive correlation (Fig. 7 & 8). Negative correlations between MgO and SiO₂, Al₂O₃, Na₂O, CaO, and K₂O (Fig. 7) are indicative of clinopyroxene and plagioclase fractionation in the ultramafic-mafic units. MgO contents with trace elements show scattered correlations with Ba, Rb, Sr, Cr, Ni, Co V, and Zr in the ultramafic-mafic suite (Fig. 8). Enrichment of Cr, Co, and Ni contents in the ultramafic-mafic units are attributed to the presence of olivine, spinel, and orthopyroxene. The alteration criterion by Polat and Hofmann (2003) is widely used to discriminate the mobility of major and trace elements of the analyzed samples. According to them, rocks characterized by Ce/Ce* ratios between 0.90 and 1.10 had experienced very little LREE mobility; on the contrary, samples having large Ce anomalies (Ce/Ce* >1.10) display high LREE mobility. In the study area, the value of Ce/Ce* ratios of peridotite varies from 0.85 to 1.01 and mafic suit ranging from 0.89 to 0.94 are indicating that they preserve their primary chemical signatures without the effect of post magmatic alteration with minor LREE mobility (Supplementary table 10)

7.3 Crustal contamination

Ghosh et al. (2019) attributed that crustal contamination is the almost predictable process for the deep-seated mantle magma derived due to the thermal erosion of magma chamber and mixing of crust and mantle melt. Based on the geochronological data, it appears that the crustal materials played a very vital role in the genesis of different varieties of granitoids associated with the mafic rocks from the eastern

margin of Singhbhum Craton (Chakraborti et al., 2019b; Chaudhuri, 2020). Crustal contamination alone cannot be considered as the sole reason for the increase of REE, Zr, and Hf concentration in the ultramafic-mafic rocks (Ramiz et al., 2018). All the analyzed samples of peridotite show variation in \sum REE contents which varies from 11.73 to 23.66 ppm (Table 5). REE plots reveal the less enriched LREE and HREE contents (Fig. 9a, b). The peridotite shows consistently low variation in the ratios of $(La/Yb)_N = 1.20-3.90$; $(La/Sm)_N = 0.97-2.96$; $(Gd/Yb)_N = 0.75-1.29$, $(Sm/Nd)_N = 0.79-2.24$, and prominent positive Eu anomalies ($Eu/Eu^* = 1.96-8.69$). The studied samples of gabbro display coherent REE patterns (Fig. 9c, d; Boynton, 1984; Sun and McDonough, 1989), low to moderate fractionation ($(La/Yb)_N = 4.43-9.65$; $(La/Sm)_N = 2.76-3.95$; $(Gd/Yb)_N = 1.22-2.48$, $(Sm/Nd)_N = 0.60-0.88$, and slightly positive Eu anomalies ($Eu/Eu^* = 0.64-1.22$). Their \sum REE contents vary from 45.78 to 188.95 ppm. The anorthositic gabbro samples also display slight enrichment in incompatible elements (LREE) over compatible HREE (Fig. 9e, f; Boynton, 1984; Sun and McDonough, 1989) and negative Eu anomalies ($Eu/Eu^* = 0.67-0.85$). Its display moderate to high variation in the ratios of $(La/Yb)_N = 5.22-20.20$; $(La/Sm)_N = 3.43-4.62$; $(Gd/Yb)_N = 1.31-2.16$, $(Sm/Nd)_N = 0.63-0.74$, and \sum REE contents vary from 51.52 to 111.88 ppm (Table 6).

Eu anomalies were noticed in ultramafic of the other cratons, which are generally attributed to secondary alteration (Sun and Nesbitt, 1978; Ludden et al., 1982; Arndt, 1994; Yadav and Das, 2017a, 2020b). Analyzed samples of peridotite display strong positive Eu anomalies are implying the involvement of continental crust during the emplacement of magma (Fig. 9a). Gabbro and anorthositic gabbro samples show slightly positive to negative Eu anomaly, moderate to high alkalis, and low anomalies of Nb which are attributing that the less role of crustal contamination during the time of magma injection (Fig. 9c to 9f; Table 6). Chukwu and Obiora (2014) proposed that the values of La/Nb ratios are more than 1.5 of the mafic and intermediate rocks, indicating the crustal contamination process. The values of La/Nb ratios show the range of 0.68-1.85 in peridotite, 1.77-4.28 in gabbro, and 1.20-5.33 in anorthositic gabbro which are attributed to the involvement of crustal contamination process (Table 6). All samples of the ultramafic-mafic suite have occupied the field of crustal contamination (Fig. 9g; Ghosh et al., 2019) whereas in La/Nb vs. SiO_2 binary plot, all the samples are showing crustal contamination with a progressive fractional crystallization trend (Fig. 9h).

7.4 Source of magma and magmatic fractionation

The nature, source, and composition of melt residues of the ultramafic-mafic rocks can be identified by using the ratios of incompatible trace elements (Fan and Kerrich, 1997; Polat et al., 1999; Rajesh et al., 2013; Teng and Santosh, 2015; Manikyamba et al., 2020). Nb-anomalies on the primitive mantle normalised multi-element spider diagram has been used to characterize different sources as well as powerful tectonic discriminants between plume and arc settings (Jochum et al., 1991; Puchtel et al., 1997). Positive Nb-anomalies suggest their derivation from the plume source that contains recycled slab material at the greatest mantle depths whereas the negative Nb-anomalies reflect the

generation of magma in arc environments or by crustal contamination processes (Polat and Kerrich, 2000; Kerrich and Xie, 2002). All the analyzed samples of the ultramafic-mafic rocks were indicated no to slight negative anomalies of Nb (Fig. 9b, d, & f) which is indicated that the suit of rocks might have derived in arc environments or by crustal contamination processes. In Nb/La vs. La/Yb binary plot indicate that the primary magma of peridotite was derived mainly from mixed lithospheric-asthenospheric mantle whereas the mafic magma was predominantly formed in the lithospheric mantle except one sample of anorthositic gabbro falls in the asthenospheric mantle field (Fig. 10a; Abdel et al., 2004). Rocks of the ultramafic-mafic suite were predominantly formed by the depleted mantle source which was confirmed through the binary plot (Fig. 10b; Geng et al., 2011). In the binary diagram of La/Sm vs. La, the peridotite following the trend of mixing or partial melting? which is corroborated by the petrographic studies where the mafic rocks follow the trend of fractional crystallization (Fig. 10c; Xia et al., 2015). The strong variation in the Eu anomalies and Sr/Y ratios between peridotite, gabbro and anorthositic gabbro reflects the fractionation of plagioclase during the crystallization in the magma chamber (Fig. 10d).

7.5 Role of garnet fractionation and condition of mantle melting

The ratios of CaO/Al_2O_3 and $(Gd/Yb)_N$ values were used by some works for the identification of garnet sources in the melt phase. The presence of garnet as a residual phase in the mantle is supported by high $CaO/Al_2O_3 (>1.0)$ and $(Gd/Yb)_N >1.0$ and low $CaO/Al_2O_3 (<1.0)$ and $(Gd/Yb)_N <1.0$ indicative of garnet entering into the melt phase (Jahn et al., 1982; Gruau et al., 1992; Yadav and Das, 2017a, 2020b). Samples of peridotite are showing $CaO/Al_2O_3 (0.77-1.95)$ and $(Gd/Yb)_N$ vary from 0.75 to 1.29, indicating the involvement of garnet as a residual phase (Fig. 11a). In the mafic suit, the values of CaO/Al_2O_3 are less than one which varies from 0.45 to 0.79 in gabbro and 0.38 to 0.59 in anorthositic gabbro whereas the values of $(Gd/Yb)_N$ vary from 1.22 to 2.48 in gabbro and 1.31 to 2.16 in anorthositic gabbro. The above-mentioned value implies varying degrees of involvement of garnet in the generation of a mafic suit of melt in the mantle (Fig. 11a). A model was proposed by Thirlwall et al. (1994) to distinguish the depth of mantle regime on the basis of HFSE ratios. The La/Yb ratios of the ultramafic-mafic rocks indicate the amount of garnet left in the restite, which supports the melting of the garnet-spinel lherzolite source (Supplementary table 10). In the binary plot of Dy/Yb vs. La/Yb, all the samples of peridotite fall spinel peridotite facies field whereas mafic suit samples come between the spinel peridotite facies and garnet peridotite facies field (Fig. 11b; Jung et al., 2006). On Sm/Yb vs. La/Sm plot, the studied rocks indicate a transitional depth from spinel to garnet melting regime with 5-25% partial melting of lherzolite (Fig. 11c; Jung et al., 2006). These studied rocks show their derivation from the deeper part of the mantle which is also supported by the REE patterns and Ce/Yb vs. Ce diagram (Fig. 11d).

7.6 Tectonic setting

The various types of the geodynamic context of ultramafic-mafic magma generation and eruption have been proposed by several workers includes; (i) ultramafic magma related to mantle plume (Kerrick and Xie, 2002; Arndt, 2003; Yadav and Das, 2017a, 2020b), (ii) ultramafic-mafic magma formed in high-degree of partial melting of a depleted-mantle source in a suprasubduction zone setting (Khatun et al., 2014), and (iii) mafic magma evolved in a continental arc setting with cogenetic and contemporaneous anorogenic granites (SBG III and Mayurbhanj granite; Manikyamba et al., 2020). In this section, we propose the models to explain the tectonic setting of the ultramafic-mafic suite of rocks within the regional geological framework of SC.

The analyzed data of ultramafic-mafic suite are plotted in different discriminating diagrams viz. R_1 - R_2 , Zr vs. Zr/Y, Zr/Y vs. Nb/Y, and Fe_2O_3 (total)- K_2O + Na_2O -MgO to depict the tectonic environments of the ultramafic-mafic suite of rocks. All the analyzed samples are plotted in the R_1 - R_2 diagram (Fig. 12a; Batchelor and Bowden, 1985), indicating that the origin of ultramafic rock by mantle-derived fractionates process whereas the pre-plate collision process is mainly responsible for the formation of the mafic suite of rocks of the study area. Samples of ultramafic fall within the field of island arc basalts whereas the mafic rocks occupy all fields of binary diagram i.e. island arc basalts, mid-ocean ridge basalts, and within-plate basalts (Fig. 12b; Pearce and Norry, 1979). In the Nb/Y vs. Zr/Y diagram (Fig. 12c; Condie, 2005), ultramafic rock mainly occupy the field of normal mid-ocean ridge basalt (NMORB) except one sample falls in the field of shallow depleted mantle (DM) whereas the mafic rocks mostly fall between the normal mid-ocean ridge basalt and arc-related basalts (ARC) except one sample fall near the primitive mantle (PM) field. The AFM ternary diagram after Beard (1986) displays that all the samples of ultramafic are occupied the field of arc-related ultramafic cumulative field whereas the mafic rocks fall in between the arc-related gabbros and arc-related mafic cumulates fields (Fig. 12d). Based on the chemical characteristics of the ultramafic-mafic suite of rocks and are enriched in SiO_2 , MgO, Ni, and Cr but low to moderate in Al_2O_3 , TiO_2 , CaO/Al_2O_3 , $(Gd/Yb)_N$, $(Sm/Yb)_N$ and $(La/Sm)_N$ ratios, low anomalies of Nb, LREE and HREE patterns attribute the derivation of these suites of rocks in continental arc setting with moderate contamination by continental crust. The genesis ultramafic-mafic suites of rocks are reasonably coincided with the widespread crustal growth event in the Singhbhum Craton.

8. Conclusion

This is the first time to present the integrated field characteristics, petrography, mineral chemistry, and geochemical studies are carried out to determine the petrogenesis and geodynamic conditions involved in the formation of the ultramafic-mafic rocks in Purnapani and Asanbani areas, Mayurbhanj district of Odisha, Singhbhum Craton, eastern India. The important conclusions drawn from the study are furnished below;

1) Three separate ultramafic bodies are delineated in the study area which is classified as peridotite. It is

mesocratic to melanocratic, medium-grained, highly foliated, and composed dominantly of mafic minerals like olivine, pyroxene, and amphibole. Towards the periphery, the rock is fine to medium-grained and highly foliated, and in the central part, it is coarse grained and less foliated. The gabbro-anorthositic gabbro suite is showing the intrusive relationship with the SBG-B and is exposed as linear and discontinuous bodies. On the basis of field observations and thin-section study, two varieties of mafic rocks were classified as gabbro and anorthositic gabbro.

- 2) The major oxide concentrations of peridotite show low SiO_2 contents ranging from 39.29 to 45.05 wt.%, Al_2O_3 (3.15-4.49 wt.%), TiO_2 (0.25-0.47 wt.%), enriched in MgO (27.41-35.25 wt.%), CaO (2.44-7.07 wt.%), LOI (4.05-8.32 wt.%), Ni (130-1700 ppm), Cr (425-8240 ppm), and V (123-260 ppm). It shows variation in $(La/Yb)_N = 1.20$ -3.90; $(La/Sm)_N = 0.97$ -2.96; $(Gd/Yb)_N = 0.75$ -1.29, $(Sm/Nd)_N = 0.79$ -2.24 ratios, $\sum REE$ (11.73-23.66 ppm), and positive Eu anomalies ($Eu/Eu^* = 1.96$ -8.69) respectively. Inversely, gabbro and anorthositic gabbro exhibit relatively higher SiO_2 , Al_2O_3 , and CaO contents and lower MgO and LOI respectively. The studied samples of gabbro and anorthositic gabbro display low to moderate fractionation $(La/Yb)_N = 4.43$ -9.65 in gabbro, 5.22-20.20 in anorthositic gabbro; $(La/Sm)_N = 2.76$ -3.95 in gabbro, 3.43-4.62 in anorthositic gabbro; $(Gd/Yb)_N = 1.22$ -2.48 in gabbro, 1.31-2.16 in anorthositic gabbro; $(Sm/Nd)_N = 0.60$ -0.88 in gabbro, 0.63-0.74 in anorthositic gabbro, Eu anomalies ($Eu/Eu^* = 0.64$ -1.22 in gabbro, 0.67-0.85 in anorthositic gabbro), and negative Nb anomalies respectively.
- 3) On the basis of mineral chemistry, petrology, and chemical data, it is proposed that these suites of rocks were derived through fractional crystallization of magma at a transitional depth of the spinel-garnet regime under the continental arc geodynamic setting with moderate contamination by continental crust.

Acknowledgments

The authors express their gratitude to the Director General, Geological Survey of India, (GSI) for permitting the publication of the paper. They are also obliged to Dr. Rajesh Asthana, former Deputy Director General, GSI, SU: Bihar for guidance and valuable suggestions during the preparation of the manuscript. They express their sincere thanks to Dr. H. Sarvothaman, Dr. L. S. Jain, and Shri R. N. Sar, former Deputy Director General, GSI, SU: Odisha, Bhubaneswar for providing necessary logistic support, supervision, and valuable technical guidance during fieldwork. Uttam Kumar Pradhan, Arya Ghosh, and B. Kusuma Kiranmayi are also acknowledged for their help during the fieldwork. This paper is the outcome of the Annual Field Season Programme (STM/ER/ORS/2009/004) of Geological Survey of India, State Unit: Odisha, Bhubaneswar.

References

- [1] Abdel-Rahman, A.F.M., Nassar, P.E., (2004). Cenozoic volcanism in the Middle East: petrogenesis of alkali basalts from northern Aparicio, A., 2010. Relationship between clinopyroxene composition and

- the formation environment of volcanic host rocks. Lebanon. *Geological Magazine* 141, 545–563.
- [2] Acharyya, S. K., Gupta, A., Orihashi, Y., (2010a). New U-Pb zircon ages from Palaeo- Mesoarchean TTG gneisses of the Singhbhum Craton, eastern India. *Geochem. Jour.* 44, 81-88. <https://doi.org/10.2343/geochemj.1.0046>.
- [3] Aldanmaz, E., (2002). Mantle source characteristics of alkali basalts and basanites in an extensional intracontinental plate setting, western Anatolia, Turkey: implications for multi-stage melting. *Int. Geol. Rev.* 44, 440–457.
- [4] Arndt, N.T., (1994). Archean komatiites. In: Condie, K.C. (Ed.), *Archean Crustal Evolution*. Elsevier, Amsterdam, pp. 11-44.
- [5] Arndt, N.T., (2003). Komatiites, kimberlites, and boninites. *J. Geophys. Res.* 108, 2293.
- [6] Batchelor, R.A., Bowden, P., (1985). Petrogenetic interpretation of granitoid rock series using multicationic parameters. *Chemical Geology* 48, 43-55.
- [7] Beard, J.S., (1986). Characteristic mineralogy of arc-related cumulate gabbros - implications for the tectonic setting of gabbroic plutons and for andesite genesis. *Geology* 14, 848-851.
- [8] Bhattacharjee, C., Mondal, S.K., (2021). Geochemistry of Fe-Ti oxide and sulfide minerals in gabbroic rocks and magnetite of the Archean Mayurbhanj Mafic Complex (eastern India): magma fractionation, thermometry and oxygen fugacity of re-equilibration, and implications for Ni-Cu mineralization. *Ore Geology Reviews*, 131, 104005.
- [9] Boynton, W.V., (1984). Geochemistry of Rare Earth Elements: Meteorite Studies. In: Henderson, P., Ed., *Rare Earth Element Geochemistry*, Elsevier, New York, 63-114. <http://dx.doi.org/10.1016/B978-0-444-42148-7.50008-3>.
- [10] Chakraborti, T.M., Ray, A., Deb, G.K., Upadhyay, D., Chakraborti, R., (2019a). Evidence of crustal reworking in the Mesoarchean: Insights from geochemical, U-Pb zircon and Nd isotopic study of a 3.08-3.12 Ga ferro-potassic granite-gneiss from northeastern margin of Singhbhum Craton, India. *Lithos* 330, 16–34.
- [11] Chakraborti, T.M., Ray, A., Deb, G.K., (2019b). Reappraisal of the ‘early proterozoic gabbro anorthosite suite’ rocks from the eastern Singhbhum craton, India: Insights from field features, petrography–mineralogy and geochemistry. *J. Earth Sys. Sci.* 128, 219.
- [12] Chaudhuri, T., (2020). A review of Hadean to Neoproterozoic crust generation in the Singhbhum Craton, India and possible connection with Pilbara Craton, Australia: the geochronological perspective. *Earth Sci. Rev.* 202, 103085.
- [13] Chaudhuri, T., Mazumder, R., Arima, M., (2015). Petrography and geochemistry of Mesoarchean komatiites from the eastern Iron Ore belt, Singhbhum craton, India, and its similarity with ‘Barberton type komatiite’. *J. Africa. Earth Sci.* 101, 135-147.
- [14] Chaudhuri, T., Satish-Kumar, M., Mazumder, R., Biswas, S., (2017). Geochemistry and Sm-Nd isotopic characteristics of the Paleoproterozoic Komatiites from Singhbhum Craton, Eastern India and their implications. *Precamb. Res.* 298, 385-402.
- [15] Chai, F.M., Zhang, Z.C., Mao, J.W., Dong, L.H., Zhang, Z.H., Wu, H., (2008). Geology, Petrology and geochemistry of the Baishiquan Ni–Cubearing mafic–ultramafic intrusions in Xinjiang, NWChina - implications for tectonics and genesis of ores. *J. Asian Earth Sci.* 31(2–4), 218-235.
- [16] Chavagnac, V., (2004). A geochemical and Nd isotopic study of Barberton komatiites (South Africa): implication for the Archean mantle. *Lithos* 75, 253-281.
- [17] Chukwu, A., Obiora, S.C., (2014). Whole-rock geochemistry of basic and intermediate intrusive rocks in the Ishiagu area: further evidence of anorogenic setting of the lower Benue rift, southeastern Nigeria. *Turkish J. Earth Sci.* 23, 427-443.
- [18] Chatterjee, S.C., (1945). The gabbro rocks found near Gorumahisani Pahar. *Proc. Nat. Inst. Sci. India*, 11, 255-282.
- [19] Chen, B., Suzuki, K., Tian, W., Jahn, B.M., (2009). Geochemistry and Os–Nd–Sr isotopes of the Gaositai Alaskan-type ultramafic complex from the northern North China craton: implications for mantle–crust interaction. *Contrib. Miner. Petrol.* 158, 683-702.
- [20] Condie, K.C., (2005). High field strength element ratios in Archean basalts: a window to evolving sources of mantle plumes? *Lithos* 79, 491-504.
- [21] Cox, K.G., Bell, J.D., Pankhurst, R.J., (1979). *The interpretation of igneous rocks*. George, Allen and Unwin, London.
- [22] Davies, J.F., Grant, R.W.E., Whitehead, R.E.S., (1979). Immobile trace elements and Archean volcanic stratigraphy in the Timmins mining area, Ontario. *Can. J. Earth Sci.* 16, 305-311.
- [23] DeWit, M.J., Tredoux, M., (1987). PGE in the 3.5 Ga Jamestown Ophiolite Complex, Barberton greenstone belt, with implications for PGE distribution in simatic lithosphere. In H.M. Prichard, P.J. Potts, J.F.W. Bowles, & S.J. Cribb (Eds.), *Proceedings of the Symposium Geo Platinum*, 87 (pp. 319–341). London and New York: Elsevier.
- [24] Dong, Y., Xiao, L., Zhou, H., Du, J., Zhang, N., Xiang, H., Wang, C., Zhao, Z., Huang, H., (2010). Volcanism of the Nanpu Sag in the Bohai Bay Basin, Eastern China: Geochemistry, petrogenesis, and implications for tectonic setting. *J. Asian Earth Sci.* 39, 173-191.
- [25] Dunn, J.A., Dey, A.K., (1942). The geology and petrology of Eastern Singhbhum and surrounding areas. *Mem. Geol. Surv. India*, 69(2), 281-456.
- [26] Falloon, T.J., Green, D.H., Danyushevsky, L.V., McNeill, A.W., (2008). The composition of near-solidus partial melts of fertile pseridotite at 1 and 1.5 GPa: Implications for the petrogenesis of MORB; *J. Pet.* 49, 591-613.
- [27] Fan, J., Kerrich, R., (1997). Geochemical characteristic of Al-depleted and undepleted komatiites and HREE-enriched tholeiites, western Abitit greenstone belt: variable HFSE/REE systematic in a heterogeneous mantle plumes. *Geochimica Cosmochimica. Acta* 61, 4723-4744.
- [28] Geng, H., Sun, M., Yuan, C., Zhao, G., Xiao, W., (2011). Geochemical and geochronological study of

- early Carboniferous volcanic rocks from the West Junggar: petrogenesis and tectonic implications. *J. Asian Earth Sci.* 42, 854-866.
- [29] Ghosh, R., Vermeesch, P., Gain, D., Mondal, R., (2019). Genetic relationship among komatiites and associated basalts in the Badampahar greenstone belt (3.25–3.10 Ga), Singhbhum Craton, Eastern India. *Precamb. Res.* 327, 196-211.
- [30] Goswami, J.N., Mishra, S., Wiedenbeck, M., Ray, S.L., Saha, A.K., (1995). 3.55 Ga old zircon from Singhbhum-Orissa iron ore craton, eastern India. *Curr. Sci.* 69, 1008-1011.
- [31] Gruau, G., Toupin, S., Fourcade, S., Blais, S., (1992). Loss of (Nd, O) and chemical (REE) memory during metamorphism of komatiites: new evidence from eastern Finland. *Contrib. Miner. Petrol.* 112, 66-82.
- [32] Herzberg, C., Zhang, J., (1996). Melting experiments on anhydrous KLB-1: Compositions of magmas in the upper mantle and transition zone; *J. Geophys. Res.* 101 8271-8295.
- [33] Himmelberg, G.R., Loney, R.A., (1995). Characteristics and petrogenesis of Alaskan-type ultramafic-mafic intrusions, Southeastern Alaska. *U S Geological Survey Professional Paper* 1564, 47.
- [34] Irvine, T., (1974). Petrology of the Duke Island ultramafic complex, southeastern Alaska. *Geol. Soc. Am. Mem.* 138, 1-240.
- [35] Jahn, B.M., Gruau, G., Glickson, A.Y., (1982). Komatiites of the Onverwacht Group, South Africa: REE chemistry, Sm-Nd age and mantle evolution. *Contrib. Miner. Petrol.* 80, 25-40.
- [36] Jayananda, M., Kano, T., Peucat, J.J., Channabasappa, S., (2008). 3.35 Ga komatiite volcanism in the western Dharwar craton, southern India: constraints from Nd isotopes and whole-rock geochemistry. *Precamb. Res.* 162, 160-179.
- [37] Jenson L.S., (1976). A new cation plot for sub-alkali volcanic rocks. *Ontario Dv. Mines. Misc. Paper no.* 66.
- [38] Jochum, K.P., Arndt, N.T., Hofmann, A.W., (1991). Nb-Th-La in komatiites and basalts: constraints on komatiites petrogenesis and mantle evolution. *Earth Planet. Sci. Lett.* 107, 272-289.
- [39] Jung, C., Jung, S., Hoffer, E., Berndt, J., (2006). Petrogenesis of Tertiary mafic alkaline magmas in the Hocheifel, Germany. *J. Petrol.* 47, 1637-1671.
- [40] Kerrich, R., Xie, Q., (2002). Compositional recycling structure of an Archaean super-plume: Nb-Th-U-LREE systematic of Archaean komatiites and basalts revisited. *Contrib. Miner. Petrol.* 142, 476-484.
- [41] Khatun, S., Mondal, S.K., Zhou, M.F., Balaram, V., Prichard, H.M., (2014). Platinum-group element (PGE) geochemistry of Mesoarchean ultramafic-mafic cumulate rocks and chromitites from the Nuasahi Massif, Singhbhum Craton (India). *Lithos*, 205, 322-340.
- [42] Leake, B.E., Woolley, A.R., Arps, C.E.S., Birch, W.D., Grice, J.D., Hawthorne, F.C., Kato, A., Kisch, H.J., Krivovichev, V.G., Linthout, K., Laird, J., Mandarino, J.A., Maresch, W.A., Nickel, E.H., Rock, N.M.S., Schumacher, J.C., Smith, D.C., Stephenson, N.C.N., Ungaretti, L., Whittaker, E.J.W., Youzhi, G., (1997). Nomenclature of amphiboles: report of the subcommittee on amphiboles of the international mineralogical association, commission on new minerals and mineral names. *The Canad. Mineral.* 35, 219-246.
- [43] Ludden, J.N., Gelin, L., Trudel, P., (1982). Archaean metavolcanics from the Rouyn-Noranda district, Abitibi greenstone belt, Quebec. 2. Mobility of trace elements and Petrogenetic constraints. *Can. J. Earth Sci.* 19, 2276-2287.
- [44] Ma, J., Lü, X., Liu, Y., Cao, X., Liu, Y., Ruan, B., Adam, M.M.A., (2016). The impact of early sulfur saturation and calc-crustal contamination on ore forming process in the Posan mafic ultramafic complex: Derived from the shallow depleted mantle, Beishan region, NW China. *J. Asian Earth Sci.* 118, 81-94.
- [45] Manikyamba, C., Pahari, A., Santosh, M., Ray, J., Sindhuja, C.S., Subramanyama, K.S.V., Singh, M.R., (2020). Mesoarchean gabbro-anorthosite complex from Singhbhum Craton, India. *Lithos*, 366-367, 105541.
- [46] Misra, S., (2006). Precambrian chronostratigraphic growth of Singhbhum-Orissa Craton, eastern Indian Shield: an alternative model. *J. Geol. Soc. India* 67, 356-378.
- [47] Misra, S., Deomurari, M.P., Wiedenbeck, M., Goswami, J.N., Ray, S., Saha, A.K., (1999). $^{207}\text{Pb}/^{206}\text{Pb}$ zircon age ages and the evolution of the Singhbhum craton, eastern India: an ion microprobe study. *Precamb. Res.* 93, 139-151.
- [48] Mitra, A., Dey, S., Zong, K., Liu, Y., Mitra, A., (2019). Building the core of a Paleoproterozoic continent: Evidence from granitoids of Singhbhum Craton, eastern India. *Precamb. Res.* 335, 105436. <https://doi.org/10.1016/j.precamres.2019.105436>.
- [49] Mondal, S.K., (2009). Chromite and PGE deposits of Mesoarchean ultramafic-mafic suites within the greenstone belts of the Singhbhum Craton (India): implication for mantle heterogeneity and tectonic setting. *J. Geol. Soc. India* 73, 1-16.
- [50] Mondal, S.K., Baidya, T.K., Rao, K.N.G., Glascock, M.D., (2001). PGE and Ag mineralization in Breccia zone of the Precambrian Nuasahi ultramafic-mafic complex, Orissa India. *Can. Mineral.*, 39, 979-996.
- [51] Mondal, S.K., Ripley, E.M., Li, C., Frei, R., (2006). The genesis of Archean chromitites from the Nuasahi and Sukinda Massifs in the Singhbhum Craton, India. *Precamb. Res.*, 148, 45-66.
- [52] Mondal, S. K., Mukherjee, R., Rosing, M.T., Frei, R., Waight, T., (2008). Petrologic, geochemical and isotopic study of 3.1 Ga peridotite chromitite suite from the western Dharwar craton (India): Evidence for recycling of oceanic crust in the Mesoarchean. *Fall Meet Suppl, Abstract EOS. Transactions of the American Geophysical Union*, 89(53). (V33C-2237).
- [53] Morimoto, N., Fabries, J., Ferguson, A.K., Ginzburg, I.V., Ross, M., Seifert, F.A., Zussman, J., Aoki, K., Gottardi, G., (1988). Nomenclature of pyroxenes. *Amer. Mineral.* 73, 1123-1133.
- [54] Mukhopadhyay, D., (2001): The Archean nucleus of Singhbhum: the present state of knowledge. *Gondwana Res.* 4, 307-318.
- [55] Mues-Schumacher, U., Keller, J., Kononova, V.A., Suddaby, P.J., (1996). Mineral chemistry and geochronology of the potassic alkaline ultramafic

- Inagli Complex, Aldan Shield, eastern Siberia. *Mineral Mag.* 60 (5), 711-730.
- [56] Mukherjee, R., Mondal, S.K., Rosing, M.T., Frei, R., (2010). Compositional variations in the Mesoproterozoic chromites of the Nuggihalli schist belt, Western Dharwar Craton (India): Potential parental melts and implication for tectonic setting. *Contrib. Miner. Petrol.* 160, 865-885.
- [57] Mukherjee, R., Mondal, S.K., Frei, R., Rosing, M.T., Waight, T.E., Zhong, H., Kumar, G.R.R., (2012). The 3.1 Ga Nuggihalli chromite deposits, Western Dharwar craton (India): Geochemical and isotopic constraints on mantle sources, crustal evolution and implications for supercontinent formation and ore mineralization. *Lithos*, 155, 392-409.
- [58] Naldrett, T., Kinnaird, J., Wilson, A., Chunnnett, G., (2008). The concentration of PGE in the earth's crust with special reference to the Bushveld Complex. *Earth Sci. Front.* 15, 264-297.
- [59] Nelson, D.R., Bhattacharya, H.N., Thern, E.R., Altermann, W. (2014). Geochemical and ion-microprobe U–Pb zircon constraints on the Archaean evolution of Singhbhum Craton, eastern India. *Precamb. Res.*, 255, 412-432.
- [60] Niu, Y., Waggoner, D.G., Sinton, J.M., (1996). Mantle source heterogeneity and melting processes beneath seafloor spreading centers: The East Pacific Rise, 18°-19°S. *J. Geophys. Res.* 101 (B12), 27711-27733.
- [61] Olierook, H.K., Clark, C., Reddy, S.M., Mazumder, R., Jourdan, F., Evans, N.J., (2019). Evolution of the Singhbhum Craton and supracrustal provinces from age, isotopic and chemical constraints. *Earth Sci. Rev.* 193, 237-259.
- [62] Pandey, O.P., Mezger, K., Ranjan, S., Upadhyay, D., Villa, I.M., Nägler, T.F., Vollstaedt, H., 2019. Genesis of the Singhbhum Craton, eastern India; implications for Archean crust-mantle evolution of the Earth. *Chem. Geol.* 512, 85-106.
- [63] Pearce J.A., Norry, M.J., (1979). Petrogenetic implications of Ti, Zr, Y and Nb variations in volcanic rocks. *Contrib. Miner. Petrol.* 69, 33-47.
- [64] Polat, A., Hofmann, A.W., (2003). Alteration and geochemical patterns in the 3.7–3.8 Ga Isua greenstone belt, West Greenland. *Precamb. Res.* 126, 197-218.
- [65] Polat, A., Kerrich, R., Wyman, D.A., (1999). Geochemical diversity in oceanic komatiites and basalts from the late Archean Wawa greenstone belts, Superior Province, Canada: trace element and Nd isotope evidence for a heterogeneous mantle. *Precamb. Res.* 94, 139-173.
- [66] Polat, A., Appel, P.W.U., Fryer, B.J., (2011). An overview of the geochemistry of Eoarchean to Mesoproterozoic ultramafic to mafic volcanic rocks, SW Greenland: Implications for mantle depletion and petrogenetic processes at subduction zones in the early Earth. *Gondwana Res.* 20 (2), 255-283.
- [67] Pradhan, U.K., Yadav, P.K., Ghosh, A., Kiranmayi, B.K., Sahoo, K.C., (2012). Final Report on the Specialised Thematic Mapping in Jashipur-Karanjia-Thakurmunda area of Badampahar-Gorumahisani belt in Mayurbhanj district, Odisha with special emphasis on PGE Mineralisation. Unpub. Rep. Geol. Surv. India F.S. 2009-12.
- [68] Prendergast, M.D., (2008). Archean komatiitic sill-hosted chromite deposits in the Zimbabwe craton. *Economic Geology* 103 (5), 981-1004.
- [69] Puchtel, I.S., Hasee, K.M., Hofmann, A.W., Chauvel, C., Kulikov, V.S., Garbe-Schonberg, C.D., Nemchin, A.A., (1997). Petrology and geochemistry of crustally contaminated komatiitic basalts from the Vetryny Belt, south-eastern Baltic continental lithosphere. *Geochimica Cosmochimica. Acta* 61, 1205-1222.
- [70] Rajesh, H.M., Chisonga, B.C., Shindo, K., Beukes, N.J., Armstrong, R.A., (2013). Petrographic, geochemical and SHRIMP U–Pb titanite age characterization of the Thabazimbi mafic sills: Extended time frame and a unifying petrogenetic model for the Bushveld Large Igneous Province. *Precamb. Res.* 230, 79-102.
- [71] Ramiz, M.M., Ali Mondal, M.E., Farooq, S.H., (2018). Geochemistry of ultramafic–mafic rocks of the Madawara Ultramafic Complex in the southern part of the Bundelkhand Craton, Central Indian Shield: Implications for mantle sources and geodynamic setting. *Geological Jour.* 1-23. DOI: 10.1002/gj.3290.
- [72] Roy, A.B., Bhattacharya, H.N., (2012). Tectonostratigraphic and geochronologic reappraisal constraining the growth and evolution of Singhbhum Archaean craton, eastern India. *J. Geol. Soc. India* 80, 455-469.
- [73] Saha, A.K., (1994). Crustal evolution of Singhbhum-North, Orissa, eastern India. *Geol. Soc. India Mem.* 27, 341.
- [74] Saha, A.K., Bose, R., Ghosh, S.N., Roy, A., (1977). Petrology and emplacement of the Mayurbhanj Granite batholith, eastern India. Evolution of the Orogenic Belts of India (Part-2), *Geol. Min. Met. Soc. India, Bull.* 49, 1-34.
- [75] Sarkar, S.N., Saha, A.K., (1962). A revision of the Precambrian stratigraphy and tectonics of Singhbhum and adjacent region. *Q. Jour. Geol. Min. Metall. Soc. India* 34, 97-136.
- [76] Sarkar, S.N., Saha, A.K., (1963). On the occurrence of two intersecting Precambrian orogenic belts in Singhbhum and adjacent areas, India. *Geol. Mag.* 100, 69-92.
- [77] Su, B.X., Qin, K.Z., Sakyi, P.A., Li, X.H., Yang, Y.H., Sun, H., Malaviarachchi, S.P., (2011). U-Pb ages and Hf-O isotopes of zircons from Late Paleozoic mafic–ultramafic units in the southern Central Asian Orogenic Belt: Tectonic implications and evidence for an Early-Permian mantle plume. *Gondwana Res.* 20 (2), 516-531.
- [78] Sun, S.S., McDonough, W.F., (1989). Chemical and isotopic systematics of oceanic basalts: implications for mantle composition and processes. In: Saunders, A.D., Norry, M.J. (Eds.), *Magmatism in the Ocean Basins*, vol. 42. Geological Society, London, pp. 313-345 (Special Publications).
- [79] Sun, S.S., Nesbitt, R.W., (1978). Petrogenesis of Archean ultrabasic and basic volcanics: evidence from rare earth elements. *Contrib. Miner. Petrol.* 65, 301-325.
- [80] Talbil, M., Bendaoud, A., Laouar, R., Ouadahi, S., (2020). Mineralogy and geochemistry of the In Allarene layered mafic-ultramafic igneous complex (In

- Ouzzal terrane, western Hoggar, South Algeria)-petrogenesis and geodynamic implications. Arab. Jour. Geosci. 13, 917. <https://doi.org/10.1007/s12517-020-05895-6>.
- [81] Tait, J., Zimmermann, U., Miyazaki, T., Presnyakov, S., Chang, Q., Mukhopadhyay, J., Sergeev, S., (2011). Possible juvenile Palaeoarchean TTG magmatism in eastern India and its constraints for the evolution of the Singhbhum craton. *Geol. Mag.* 148 (2), 340-347.
- [82] Teng, X., Santosh, M., (2015). A long-lived magma chamber in the Paleoproterozoic North China Craton: evidence from the Damiao gabbro-anorthosite suite. *Precamb. Res.* 256, 79-101.
- [83] Thirlwall, M.F., Upton, B.G.J., Jenkins, C., (1994). Interaction between continental lithosphere and the Iceland plume-Sr-Nd-Pb isotope geochemistry of Tertiary basalts, NE Greenland. *J. Petrol.* 35, 839-879.
- [84] Tistl, M., (1994). Geochemistry of platinum-group elements of the zoned ultramafic Alto Condoto Complex, Northwest Colombia. *Econ. Geol.* 89, 158-167.
- [85] Upadhyaya, D., Chattopadhyaya, S., Kooijmanb, E., Mezger, K., Berndt, J., (2014). Magmatic and metamorphic history of Paleoproterozoic trondhjemite-granodiorite (TTG) suite from the Singhbhum craton, eastern India. *Precamb. Res.* 252, 180-190.
- [86] Winchester, J.A., Floyd, P.A., (1977). Geochemical discrimination of different magma series and their differentiation products using immobile elements. *Chem. Geol.* 20, 325-343.
- [87] Xia, Y., Xu, X., Zhao, G., Liu, L., (2015). Neoproterozoic active continental margin of the Cathaysia block: evidence from geochronology, geochemistry, and Nd-Hf isotopes of igneous complexes. *Precamb. Res.* 269, 195-216.
- [88] Yadav, P.K., (2017c). Incidence of uranium and thorium mineralization in quartz-pebble conglomerate of Koira Group, Singhbhum Craton, India. *Inter. Jour. Res. Anal. Rev.* 4 (4), 484-488.
- [89] Yadav, P.K., Pradhan, U.K., Mukherjee, A., Sar, R.N., Sahoo, P., Das, M., (2015). Basic characterization of Kapili Komatiite from Badampahar-Gorumahisani Schist Belt, Singhbhum Craton, Odisha, India. *Indian Jour. Geosci.* 69 (1), 1-12.
- [90] Yadav, P.K., Sahoo, P., Pradhan, U.K., Das, M., (2016). Komatiite from Mesoarchean Badampahar-Gorumahisani greenstone belt, Singhbhum craton, eastern India: Petrogenetic affinity with 'Barberton type'. 35th Inter.Geosci.Congress., Cape Town, South Africa.
- [91] Yadav, P.K., Das, M., (2017a). Petrology, geochemistry and petrogenesis of Al-depleted komatiite from Badampahar-Gorumahisani Greenstone Belt of Eastern Iron Ore Group, Singhbhum Craton, India. *Indian Jour. Geosci.* 70(3 & 4) & 71(1), 313-328.
- [92] Yadav, P.K., Das, M., (2017d). Geochemistry of Kapili Komatiite from Badampahar-Gorumahisani greenstone belt, Singhbhum craton, India and its resemblance with 'Barberton Komatiite.' *Inter. Jour. Res. Anal. Rev.* 4 (4), 495-507.
- [93] Yadav, P.K., Das, M., (2019a). Geochemistry of Mesoarchean felsic tuff from Bonai-Kendujhar belt of Western Iron Ore Group, Singhbhum Craton, India: implications for volcanic arc tectonic setting. *Indian Jour. Geosci.* 73 (1), 1-14.
- [94] Yadav, P.K., Das, M., Ray, S., (2020a). Petrochemical signatures of meta-andesite from Badampahar-Gorumahisani Greenstone Belt, Singhbhum Craton: Implication on Precambrian tectonic setting of the Eastern India Shield. *Indian Jour. Geosci.* 74 (1), 22-39.
- [95] Yadav, P.K., Das, M., (2020b). Komatiite from Eastern Iron Ore Group, Singhbhum Craton, India: Implication for Mantle Plume - Arc Tectonic Setting. *Inter. Jour. Sci. Res.* 9 (8), 656-672. <https://doi.org/10.21275/SR20810161355>.
- [96] Yang, S.H., Zhou, M.F., (2009). Geochemistry of the ~430-Ma Jingbulake mafic-ultramafic intrusion in Western Xinjiang, NM China: implications for subduction related magmatism in the South Tianshan orogenic belt. *Lithos* 113, 259-273.
- [97] Yellappa, T., Venkatasivappa, V., Koizumi, T., Chetty, T.R.K., Santosh, M., Tsunogae, T. (2014). The mafic-ultramafic complex of Aniyapuram, Cauvery Suture Zone, southern India: Petrological and geochemical constraints for Neoproterozoic suprasubduction zone tectonics. *J. Asian Earth Sci.* 95, 81-98.
- [98] Zhu, W.G., Zhong, H., Hu, R.Z., Liu, B.G., He, D.F., Song, X.Y., Deng, H.L., (2010). Platinum-group minerals and tellurides from the PGE-bearing Xinjie layered intrusion in the Emeishan Large Igneous Province, SW China. *Mineral. Petrol.* 98, 167-180. <https://doi.org/10.1007/s00710-009-0077-y>.

Figure Captions

Fig. 1: (a) Tectonic map of India, (b) Generalized geological map of central Singhbhum Craton, North Odisha showing location of the study area (modified after Saha, 1994; Yadav and Das, 2020b).

Fig. 2: Geological map of the study area showing the occurrence of ultramafic-mafic rocks belonging to the Intrusive Unit, Mayurbhanj district, Odisha, eastern part of Singhbhum Craton, India (modified after Pradhan et al., 2012).

Fig. 3: (a) Outcrop of foliated peridotite, south of Purnapani. (b) Foliated peridotite showing steeping dip towards SE, northeast of Asanbani. (c) Peridotite is mesocratic to melanocratic, coarse to very coarse-grained, and chiefly composed of pyroxenes, north of Asanbani. (d) Outcrop of gabbro, south of Purnapani. (e) The encrustation of vanadiferous-titanium-magnetite was observed in the central part of the gabbro body, south of Purnapani. (f & g) Anorthositic gabbro is generally massive, undeformed, coarse to very coarse-grained, and predominantly made up of plagioclase and pyroxenes, east of Asanbani.

Fig. 4: (a) Relict grains of olivine are preserved in the felty mass of serpentine in peridotite. (b) Mesh texture formed due to the breakdown of olivine into serpentine and secondary magnetite which is corroborated by the backscattered electron image (BSE) in peridotite. (c) Cumulus texture defines by two types of

pyroxenes in peridotite. **(d)** The ophitic and sub-ophitic textures are defined by the early formed cumulus phase of plagioclase crystals that are fully or partially enveloped by the pyroxene crystals in gabbro. **(e & f)** Grains of inverted pigeonite are noticed in gabbro which is confirmed by the BSE image. **(g)** The conversion of augite into hornblende is noticed in anorthositic gabbro. **(h)** The plagioclase crystals show euhedral habit with bent lamellar twinning, indicating the deformation signatures of anorthositic gabbro.

Abbreviations: Ol- Olivine; Srp- Serpentine; Aug- Augite; En- Enstatite; Hyp- Hypersthene; Pl- Plagioclase; Hbl- Hornblende; Qz- Quartz; Ser- Sericite.

Fig. 5: **(a)** Olivine of peridotite falls in the chrysolite field. **(b)** Classification diagram of the composition of pyroxenes of the peridotite, gabbro, and anorthosite when plotted in the Wo-En-Fs diagram (Morimoto et al., 1988). **(c)** Depicting the amphiboles composition of peridotite and anorthositic gabbro while using the binary diagram of Leake et al. (1997). **(d)** Plagioclase composition of the gabbro and anorthositic gabbro on the Or-Ab-An triangle diagram. (Peridotite- solid triangle with green; Gabbro- solid circle with red; Anorthositic gabbro- solid triangle with purple).

Fig. 6: **(a)** Al_2O_3 - Fe_2O_3 + TiO_2 - MgO cationic ternary diagram for the ultramafic-mafic rocks (Jensen, 1976). **(b)** The binary plot of Na_2O+K_2O vs. SiO_2 (Cox et al., 1979) in which the studied samples of mafic rocks have occupied the fields of gabbro. **(c)** Nb/Y vs. SiO_2 diagram in which the studied samples of mafic rocks are falling in subalkaline basalt and andesite fields (Winchester and Floyd, 1977). **(d)** Ternary plot of TiO_2 -Y+Zr-Cr in which the samples of peridotite show enrichment of magnesium whereas, the mafic suit depicts the tholeiitic to the calc-alkaline character (Davies et al., 1979). (Symbols used in plots: ■ - Peridotite; ● - Gabbro; ▲ - Anorthositic gabbro).

Fig. 7: Plots of ultramafic-mafic suite in variation diagrams for major oxides plotted against MgO (Same symbols used in Fig. 6).

Fig. 8: Selected trace elements vs. MgO plots of ultramafic-mafic suite (Same symbols used in Fig. 7).

Fig. 9: **(a & b)** Chondrite normalized REE and primitive mantle normalized multi-element diagrams of peridotite (Boynton, 1984; Sun and McDonough, 1989). **(c to f)** Chondrite normalized REE and primitive mantle normalized multi-element diagrams of gabbro and anorthositic gabbro showing flat to slight fractionation of LREE with flat HREE. **(g)** Binary plot of Zr vs. Y indicate the involvement of the crustal contamination process. **(h)** SiO_2 vs. La/Nb showing assimilation with fractional crystallization trend (Dong et al., 2010). (Same symbols used in Fig. 8).

Fig. 10: **(a)** La/Yb vs. Nb/La depicts that the primary magma of the ultramafic-mafic rocks were derived in between lithospheric mantle and mixed lithospheric-asthenospheric mantle. **(b)** The depleted mantle source depicts through Zr and Nb relationship. **(c)** La vs. La/Sm binary plot indicates fractional crystallization is the key process for the generation of the studied rocks. **(d)** Eu/Eu* vs. Sr/Y diagram displays the plagioclase fractionation (Xia et al., 2015).

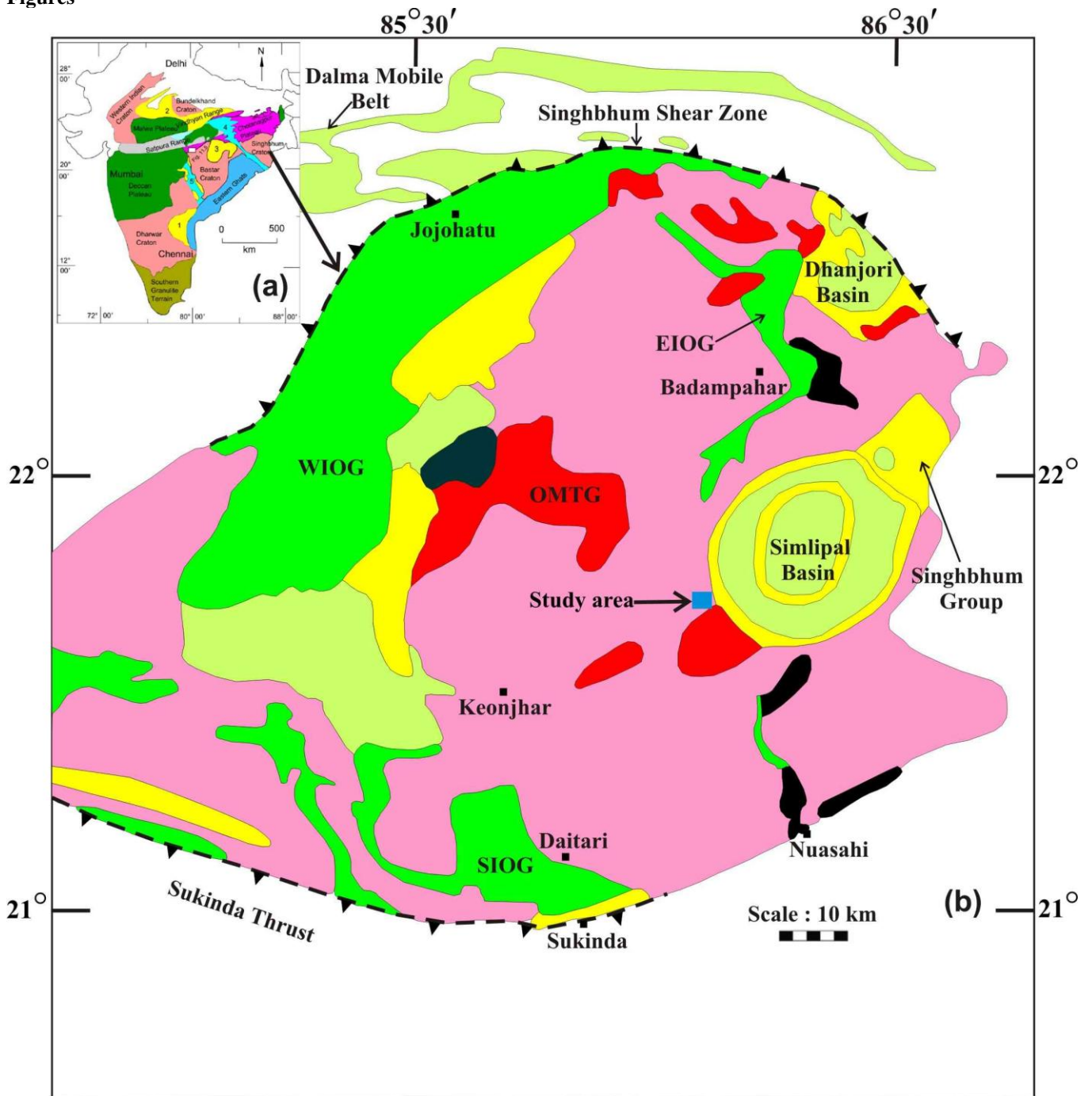
Fig. 11: **(a)** Samples of the ultramafic-mafic suite are plotted in $(Gd/Yb)_N$ vs. CaO/Al_2O_3 diagram in which most samples fall in the garnet fractionation field. **(b)** La/Yb vs. Dy/Yb

plot, reflecting on spinel to garnet-peridotite facies transitional melting regime. **(c)** In a binary plot of La/Sm vs. Sm/Yb, all the samples fall in a spinel garnet lherzolite field (Aldanmaz, 2002). Dashed lines are melting trends in figure b and c. **(d)** Ce vs. Ce/Yb plot for the ultramafic-mafic rocks (Niu et al., 1996).

Fig. 12: **(a)** Analyzed samples occupy the fields of mantle-derived fractionates whereas the pre-plate collision while plotting in R_1 vs. R_2 diagram. **(b & c)** Ultramafic-mafic samples are plotted in Zr vs. Zr/Y and Nb/Y vs. Zr/Y diagrams for depicting the tectonic environment. **(d)** The AFM ternary diagram after Beard (1986), indicating that the ultramafic are occupied the field of arc-related ultramafic cumulative field whereas the mafic rocks fall in between the arc-related gabbros and arc-related mafic cumulates fields.

(Abbreviations: IAT, island arc tholeiites; MORB, mid-ocean ridge basalts; CAB, continental arc basalts; WPB, within plate basalt; UC, upper continental crust; PM, primitive mantle; DM, shallow depleted mantle; HIMU, high mu (U/Pb) source; EM1 and EM2, enriched mantle sources; ARC, arc-related basalts; NMORB, normal mid-ocean ridge basalt; OIB, oceanic island basalt; DEP, deep depleted mantle; EN, enriched component; REC, recycled component).

Figures



INDEX









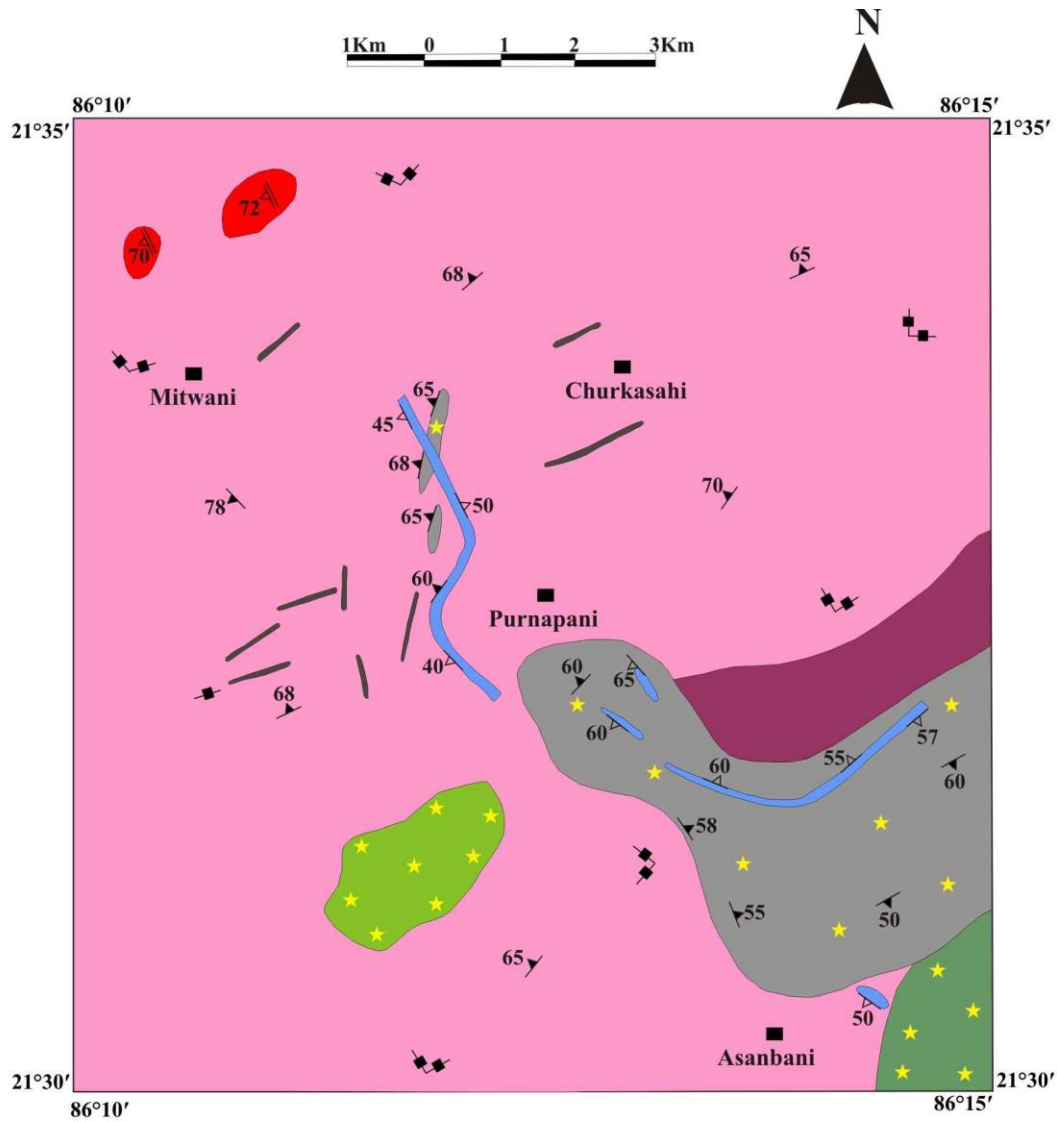
- | | |
|---|---|
|  Granitoid batholithic complex (3.3-3.1Ga) |  Ultramafic-Mafic rocks with chromitite-PGE deposits (3.3-3.1Ga) |
|  OMTG Tonalite-Granodiorite (3.29Ga) |  Late Archean-Proterozoic sedimentary sequence |
|  OMTG Supracrustal (3.3Ga) |  Late Archean-Proterozoic volcanic sequence |
|  Iron Ore Group greenstone sequences with BIF (>3.1Ga) |  Study area |

Figure 1



INDEX

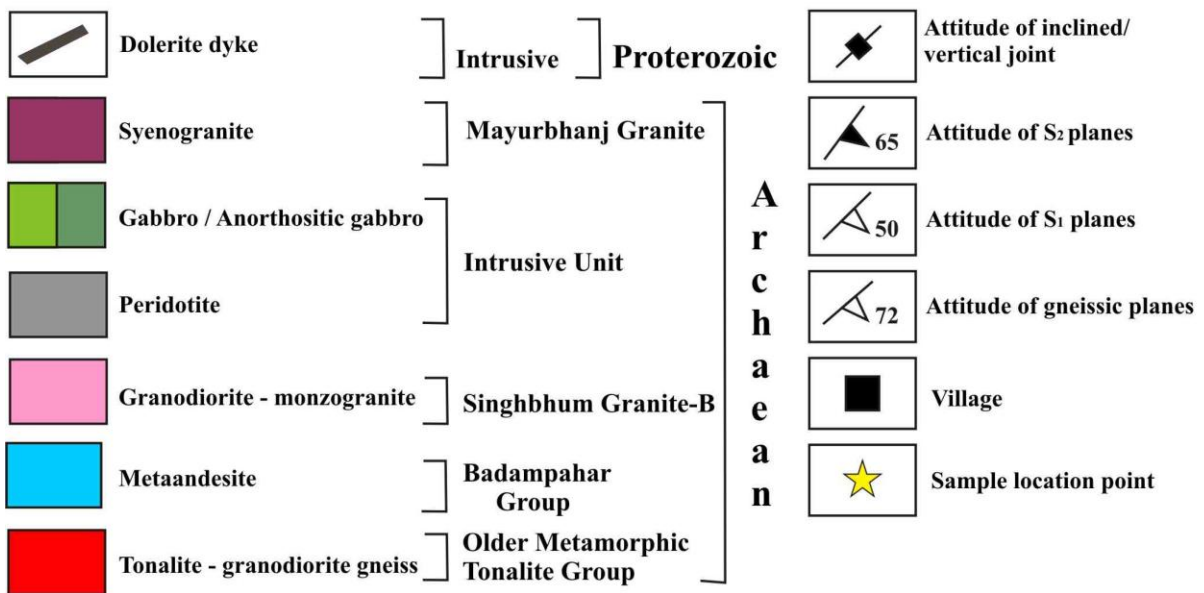


Figure 2



Figure 3

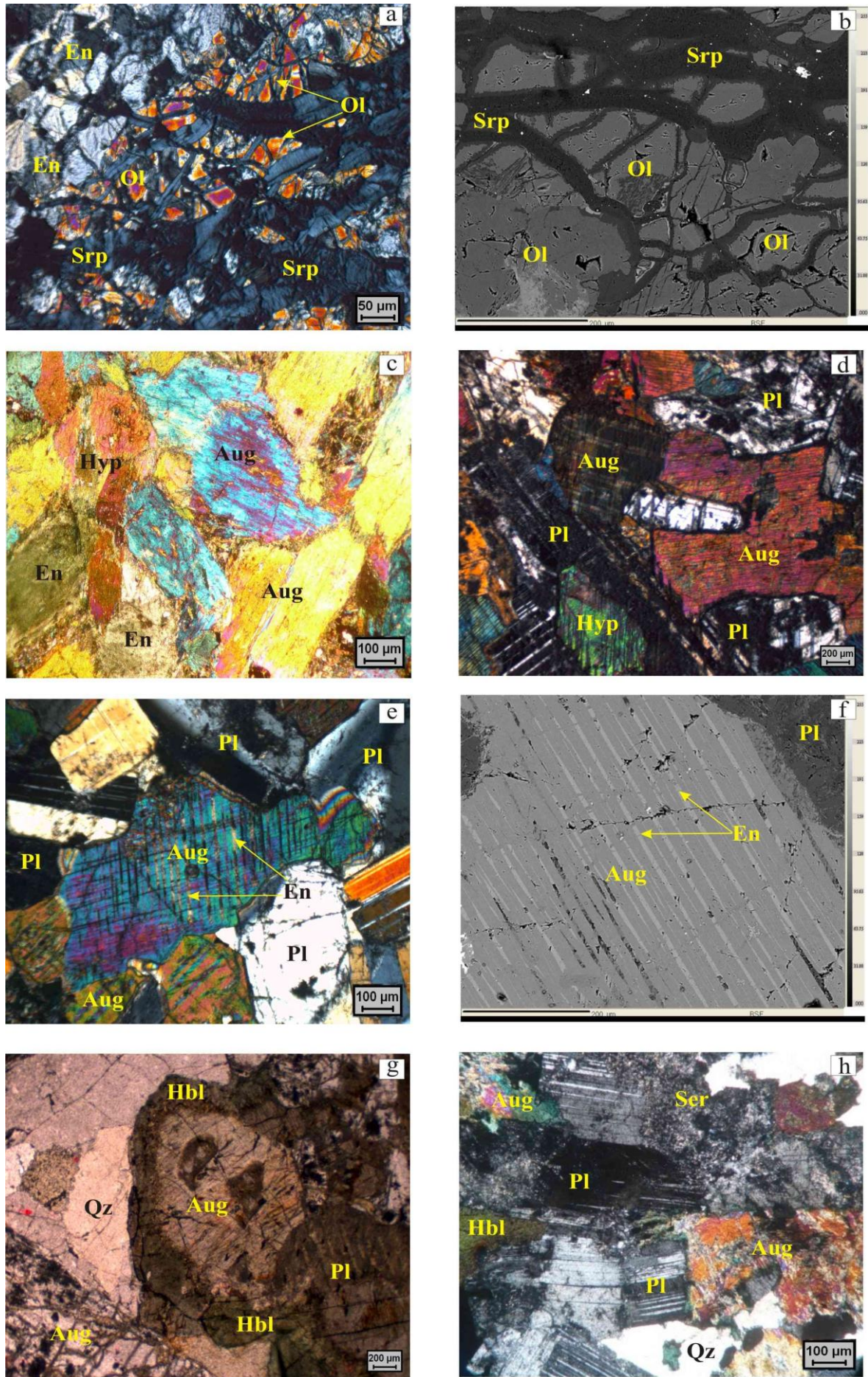


Figure 4

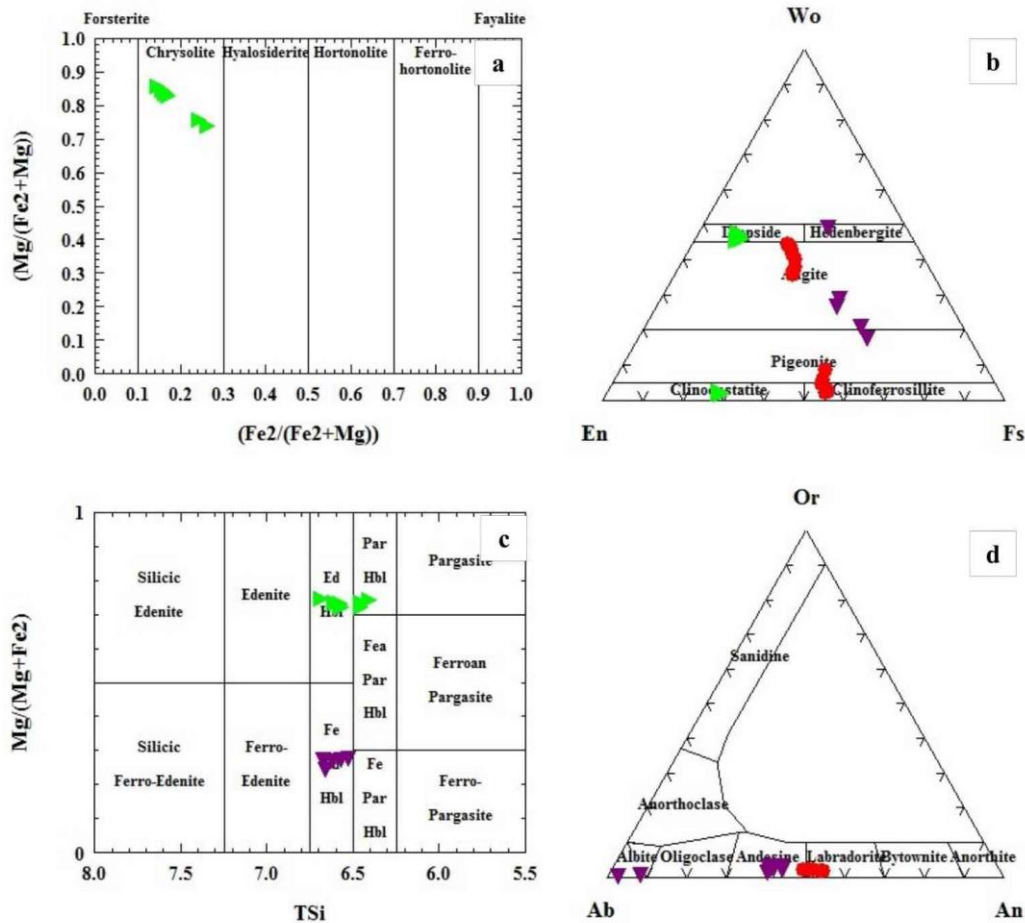


Figure 5

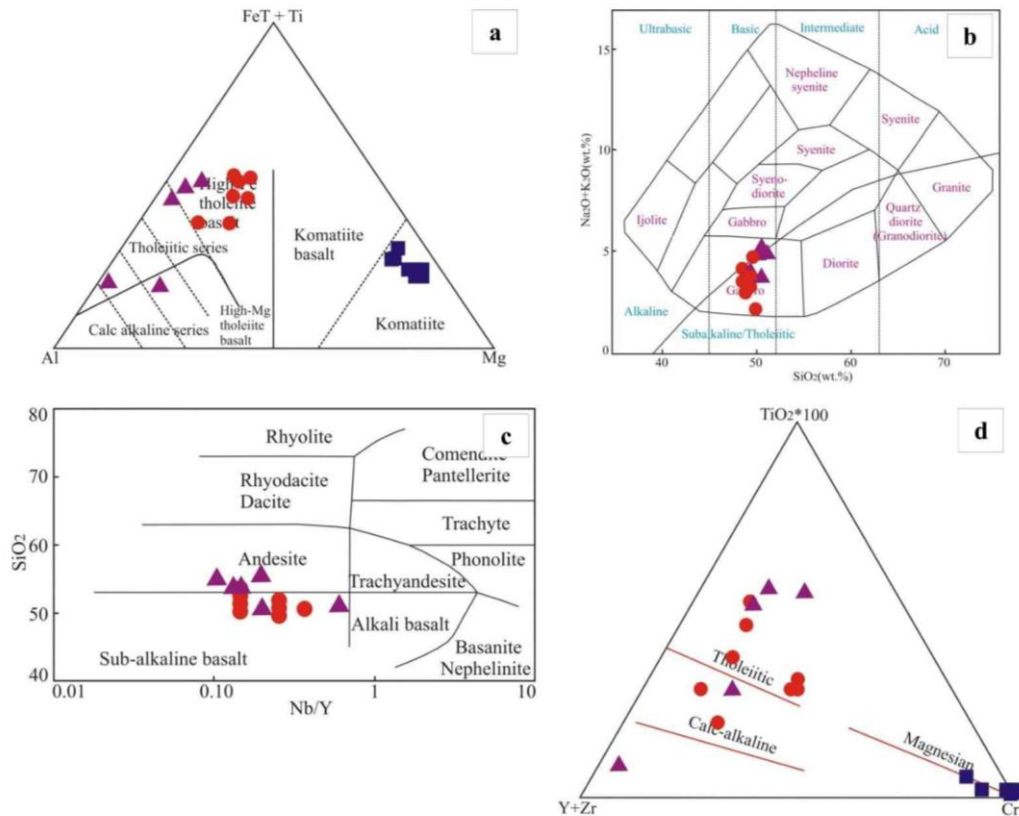


Figure 6

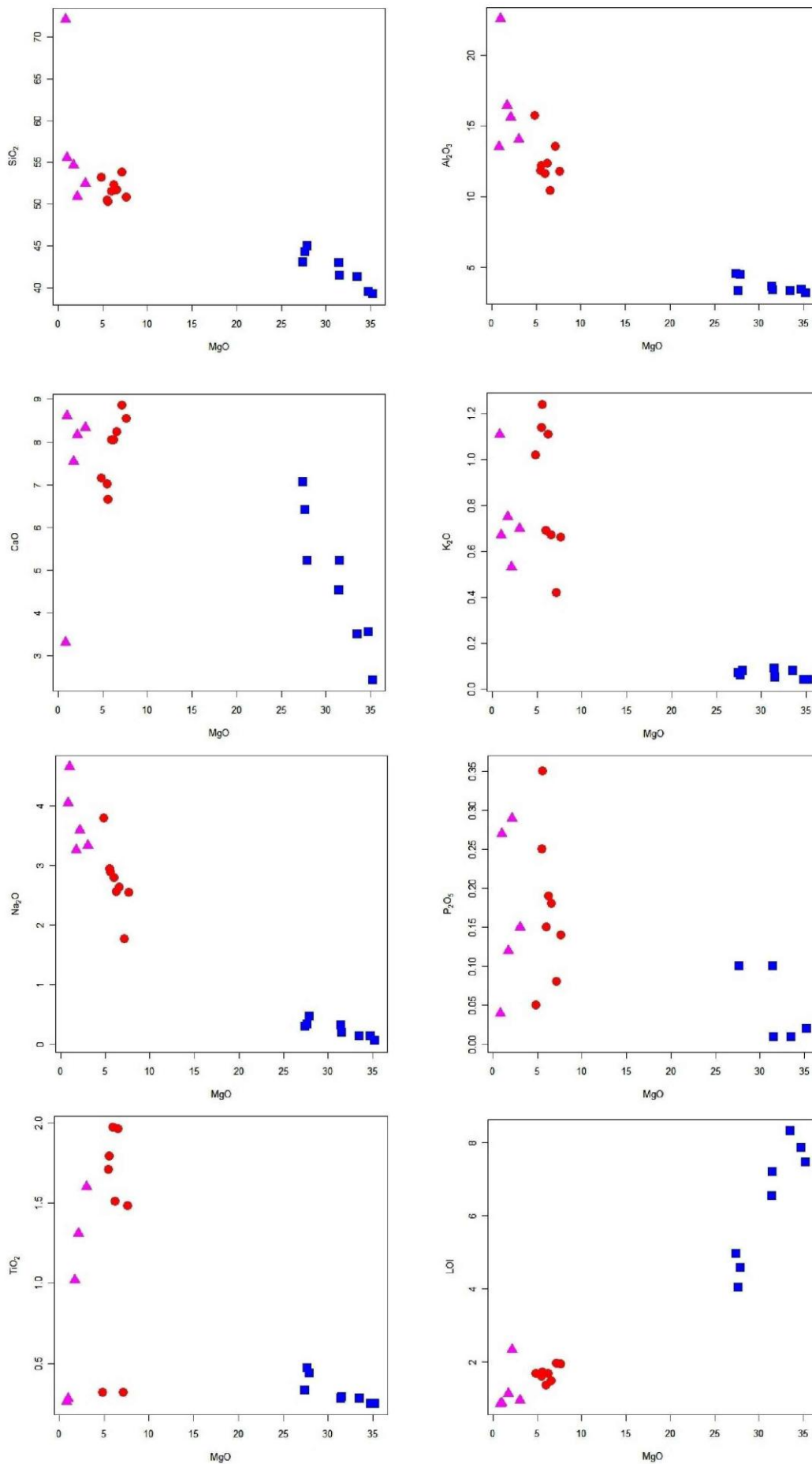


Figure 7

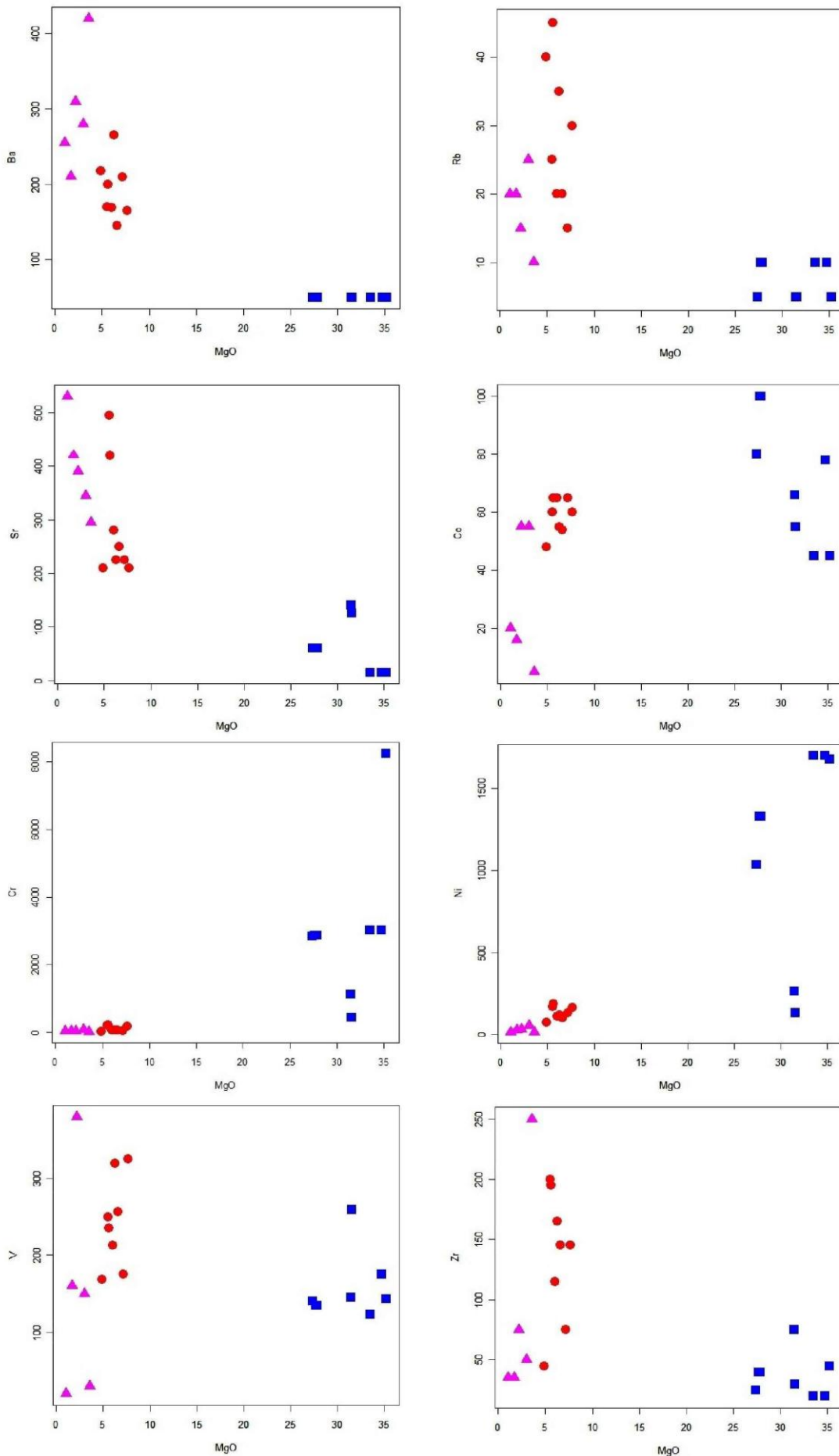


Figure 8

Volume 11 Issue 12, December 2022

www.ijsr.net

Licensed Under Creative Commons Attribution CC BY

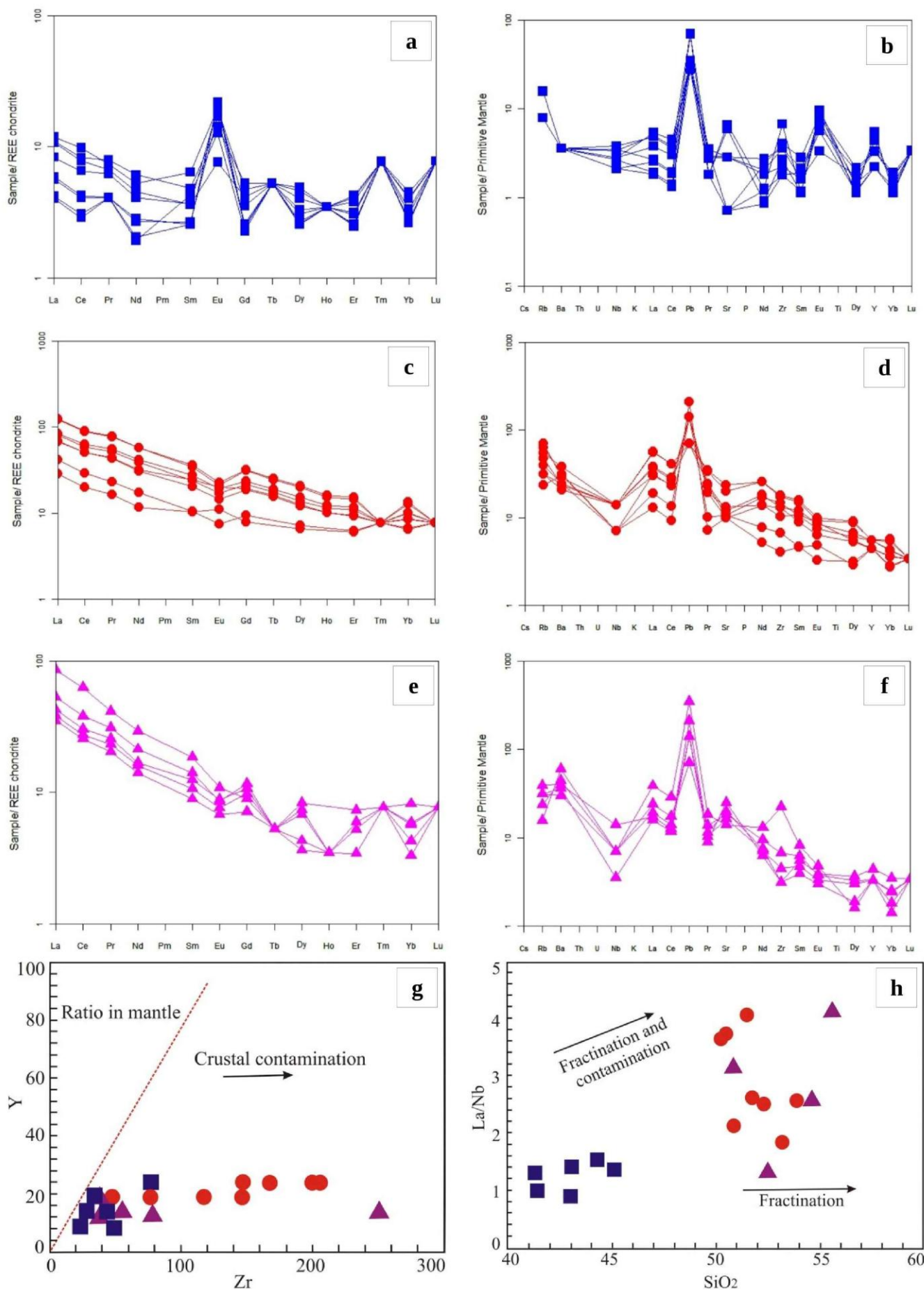


Figure 9

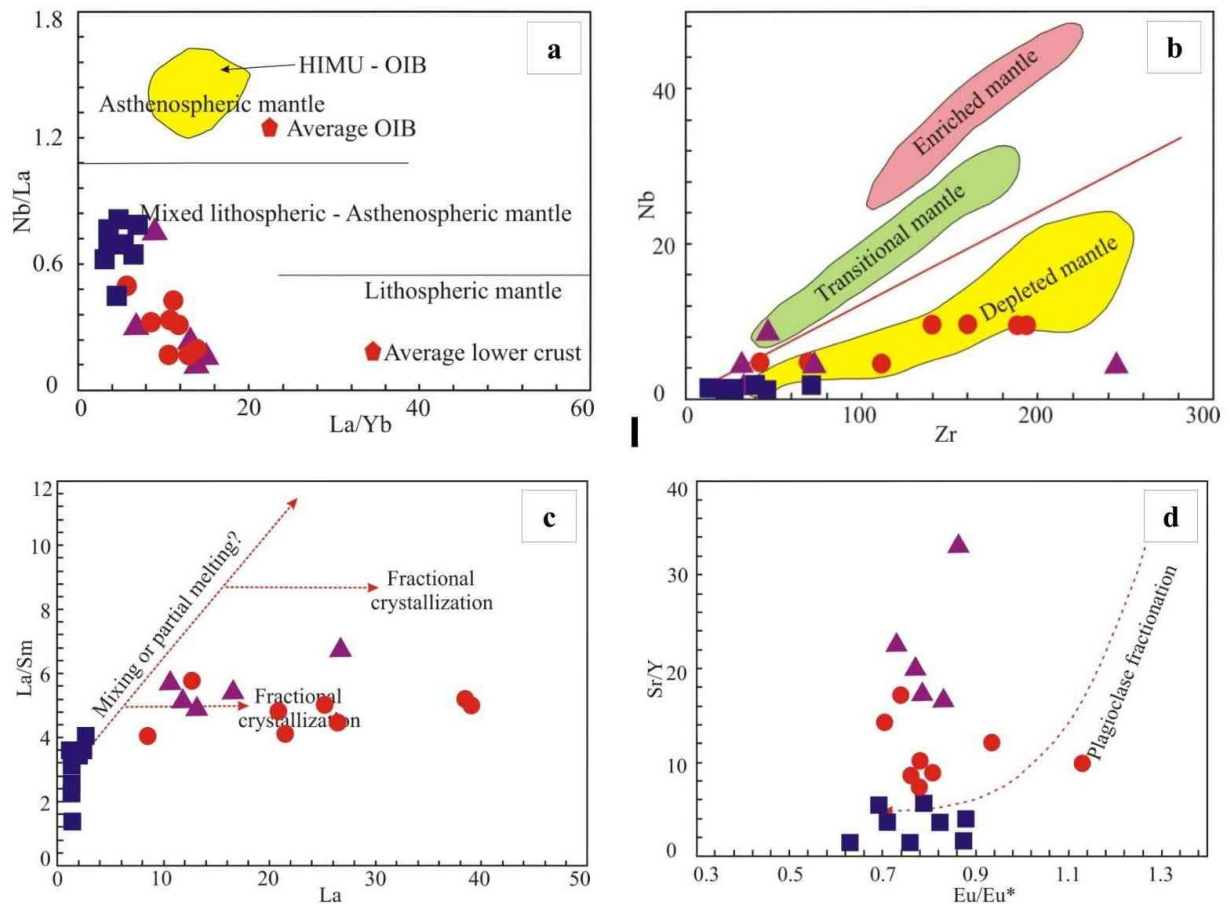


Figure 10

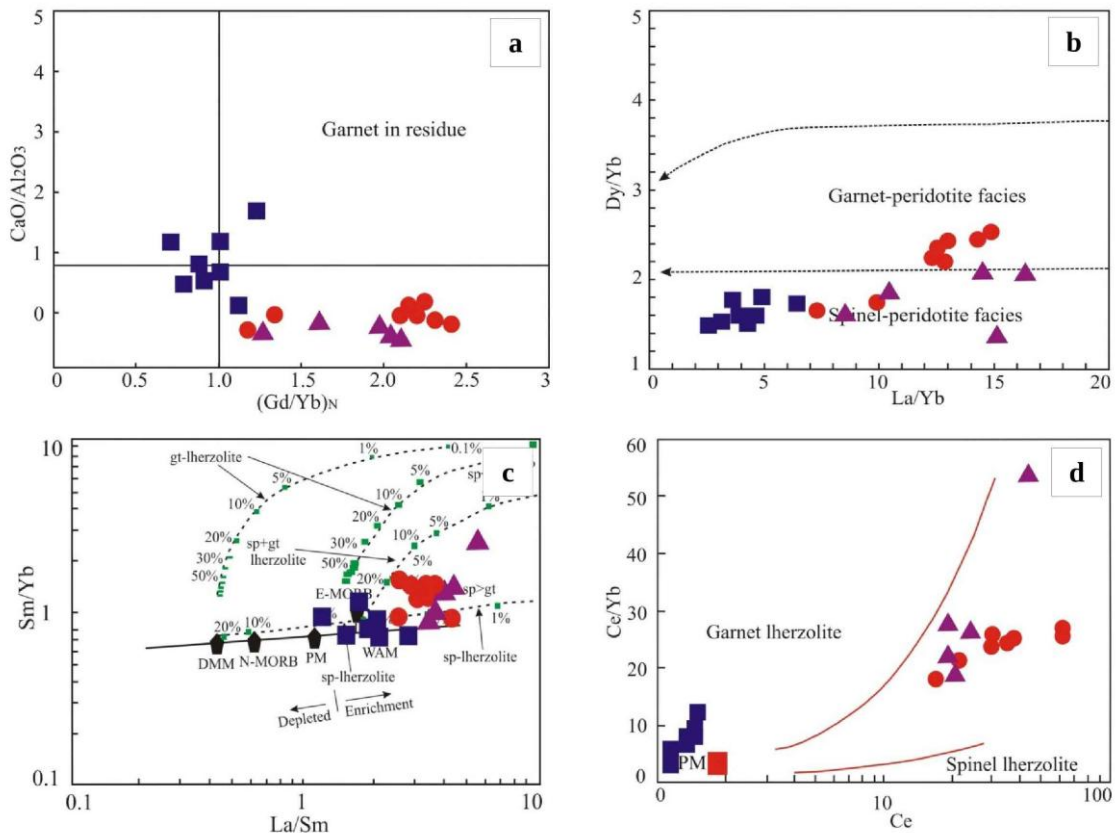


Figure 11

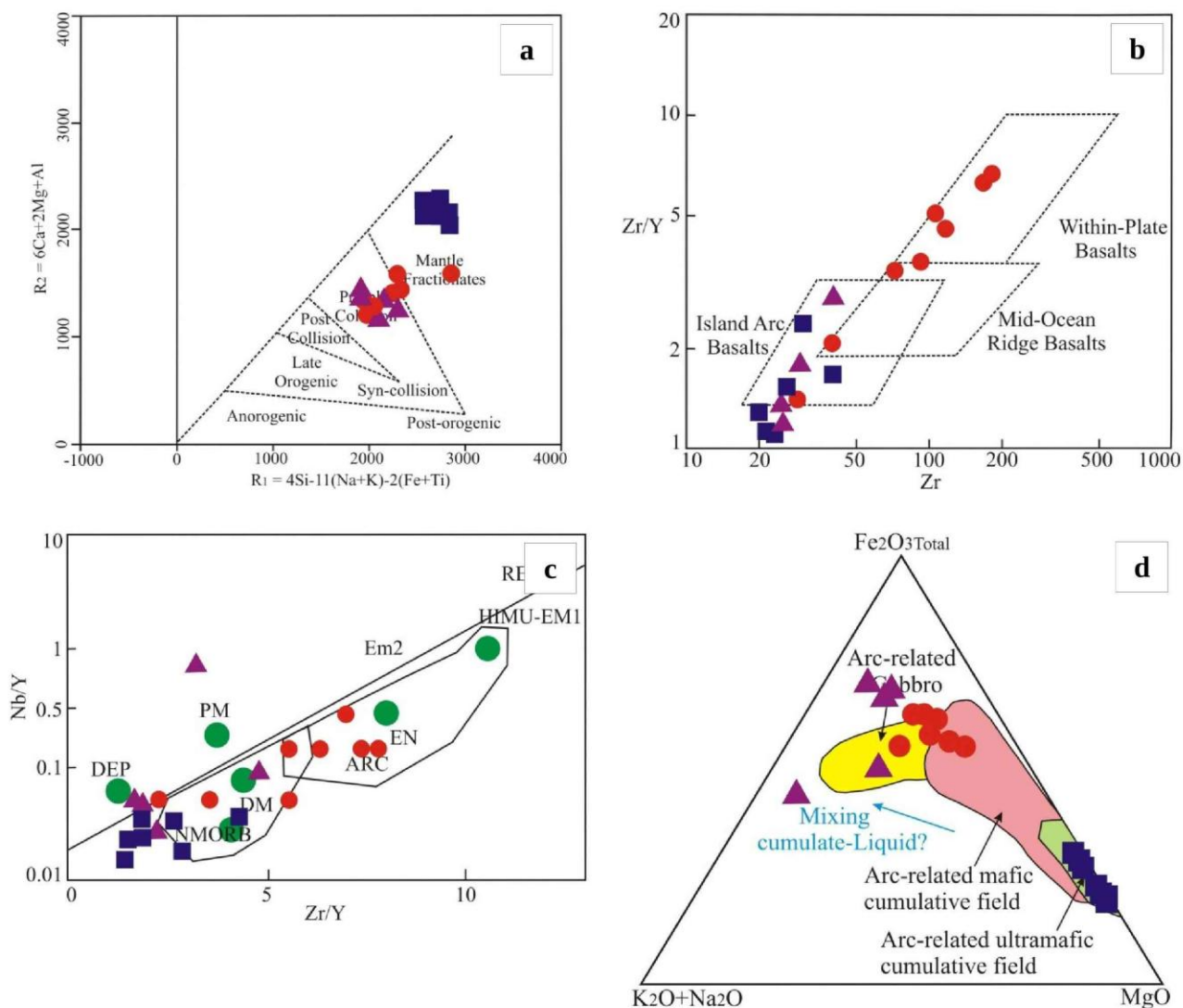


Figure 12

Tables

Table 1: Regional stratigraphic sequence of Singhbhum Craton, India (after Saha, 1994; Ghosh et al., 2019; Manikyamba et al., 2020)

Stratigraphic unit	Events	Major lithologies	Age (Ga)
		Metamorphism of OMG, OMTG and SBG II and III	3.02-2.96, 2.52 and 1.06
Mayurbhanj granite and gabbro	Coeval emplacement of granite and gabbro	Granite, Gabbro Anorthosite	3.09-3.08 3.12
Simlipal lava and metasediments	Formation of Volcano sedimentary basin	Spillites, tuffs, quartzite	~>3.09
Unconformity			
Thermal Metamorphism of OMTG due to emplacement of SBG Type - III, Bonai granite			
SBG Type - III Bonai granite	Emplacement of granitic pluton	Granodiorite to granite Granite to granodiorite	3.12 3.16
Metamorphism of SBG Type - I, OMTG and OMG			
Iron Ore Group	Deposition and metamorphism of Iron ore group of rocks	Mafic to felsic volcanic rocks, tuff, banded iron formations, local dolomite, quartzitic sandstone and conglomerate	3.19-3.13 3.3-3.1
Unconformity			
Metamorphism of SBG Type - I & II, OMTG and OMG			
Kaptipada granite		Granite, tonalite	~3.29
SBG Type - II	Emplacement of granitic pluton	Granite, tonalite and granodiorite	3.35
SBG Type - I	Emplacement of granitoid plutons	Tonalite, granodiorite	3.44
Metamorphism of OMTG and OMG			
			3.40

OMTG granite		Granite	3.32
OMTG	Intrusion of tonalite-trondhjemite-granodiorite rocks in OMG	Tonalite gneiss and granodiorite	3.44 and 3.52
OMG	Deposition of sediments with volcanics	Amphibolites, pelitic schists, banded calc-gneiss	3.55-3.44
Unconformity			
Unpreserved primitive crust represented by xenocrystic zircons present in younger rocks			3.60-3.55, 3.61, 4.24-4.05

Table 2: Representing Electron Probe Microanalysis (EPMA) of olivine, pyroxene and amphibole from peridotite

Olivine								
Oxide wt. %	TK139/1	TK139/2	TK139/3	TK139/4	TK139/5	TK139/6	TK139/7	TK139/8
Al ₂ O ₃	0.007	0.02	0.007	0.005	0.238	0.022	0.132	0.321
P ₂ O ₅	0.034	0.012	0.034	0.012	0.032	0	0.042	0.042
K ₂ O	0.119	0.082	0.004	0.009	0.033	0.059	0.089	0.079
TiO ₂	0.046	0.007	0.033	0.044	0.018	0.091	0.009	0.019
Cr ₂ O ₃	0.012	0.012	0.009	0.077	0.024	0.05	0.019	0.019
MnO	0.49	0.544	0.148	0.17	0.197	0.196	0.194	0.124
FeO	21.881	20.078	14.2	16.786	15.351	18.567	15.678	15.108
CaO	0.04	0.133	0.041	0.057	0.119	0.063	0.068	0.068
SiO ₂	37.858	34.685	39.004	37.652	38.046	37.236	39.008	37.008
Na ₂ O	0.115	0.135	0.145	0.111	0.166	0.299	0.269	0.269
MgO	38.976	43.356	45.356	44.131	45.234	43.912	43.728	46.234
NiO	0.417	0.381	0.283	0.225	0.253	0.31	0.333	0.333
Total	99.995	99.445	99.264	99.279	99.711	100.805	99.569	99.624
Cations and end members (4 Oxygen)								
Si	1.031	0.996	0.997	0.987	1.007	0.967	1.005	0.978
Al	0	0.001	0	0	0.008	0.001	0.004	0.01
Ti	0.001	0	0.001	0.001	0	0.002	0	0
Fe ₂	0.499	0.482	0.32	0.327	0.303	0.337	0.282	0.343
Mn	0.011	0.013	0.003	0.004	0.005	0.004	0.004	0.003
Mg	1.41	1.493	1.67	1.685	1.653	1.703	1.68	1.665
Ca	0.001	0.004	0.001	0.002	0.003	0.002	0.002	0.002
Na	0.006	0.008	0.008	0.006	0.009	0.015	0.013	0.014
K	0.004	0.003	0	0	0.001	0.002	0.003	0.003
Ni	0.009	0.009	0.006	0.005	0.006	0.006	0.007	0.007
Cations	2.972	3.009	3.006	3.017	2.995	3.039	3	3.025
Fe_FeMg	0.26	0.24	0.16	0.16	0.15	0.17	0.14	0.17
Mg_FeMg	0.74	0.76	0.84	0.84	0.85	0.83	0.86	0.83
Pyroxene								
Oxide wt. %	TK139/1	TK139/2	TK139/3	TK139/4	TK139/5	TK139/6	TK139/7	TK139/8
Al ₂ O ₃	1.502	1.475	1.147	1.167	1.063	1.064	1.041	0.945
P ₂ O ₅	0	0	0.049	-0.009	0.036	0	-0.019	-0.066
K ₂ O	-0.012	-0.016	-0.002	0.003	0.022	-0.011	-0.007	-0.002
TiO ₂	0.093	0.045	0.04	0.044	0.036	0.116	-0.014	-0.011
Cr ₂ O ₃	0.131	0.148	0.168	0.083	0.193	0.107	0.078	0.071
MnO	0.124	0.274	0.369	0.175	0.211	0.372	0.4	0.315
FeO	6.916	6.975	18.063	5.841	6.395	18.167	20.545	22.027
CaO	23.982	24.567	1.217	25.678	24.356	0.885	0.864	0.916
SiO ₂	50.731	50.345	52.815	51.289	50.267	51.64	52.126	50.367
Na ₂ O	0.199	0.223	0.038	0.159	0.168	0.011	0.024	0.005
MgO	15.499	15.033	26.186	15.789	16.784	27.689	25.178	24.754
NiO	-0.016	0.092	0.073	-0.045	0.052	0.025	0.161	0.103
Total	99.149	99.161	100.163	100.174	99.583	100.065	100.377	99.424
Cations and end members (6 Oxygen)								
TSi	1.884	1.892	1.917	1.927	1.901	1.951	1.95	1.935
TAl	0.066	0.067	0.049	0.054	0.048	0.047	0.045	0.043
M1Al	0	0	0	0	0	0	0	0
M1Ti	0.003	0.001	0.001	0.001	0.001	0.003	0	0
M1Fe ₂	0.136	0.13	0	0.143	0.097	0	0	0
M1Cr	0.004	0.004	0.005	0.003	0.006	0.003	0.002	0.002
M1Mg	0.858	0.861	0.992	0.855	0.894	0.993	0.993	0.995
M1Ni	0	0.003	0.002	-0.001	0.002	0.001	0.005	0.003
M2Mg	0	0	0.425	0	0	0.396	0.398	0.42
M2Fe ₂	0.079	0.094	0.548	0.048	0.109	0.558	0.558	0.553
M2Mn	0.004	0.009	0.011	0.006	0.007	0.012	0.013	0.01
M2Ca	0.954	0.922	0.047	0.953	0.921	0.036	0.034	0.038

M2Na	0.014	0.017	0.003	0.012	0.013	0.001	0.002	0	
M2K	-0.001	-0.001	0	0	0.001	-0.001	0	0	
Sum_cat	4.001	4.001	4	4	3.999	4.001	4	4	
Ca	46.983	45.712	2.338	47.564	45.404	1.796	1.719	1.889	
Mg	42.249	42.725	70.01	42.644	44.084	69.623	69.691	70.183	
Fe2_Mn	10.768	11.563	27.652	9.792	10.512	28.581	28.59	27.928	
JD1	0	0	0	0	0	0	0	0	
AE1	0.674	0.783	0.128	0.605	0.671	0.014	0.07	0.014	
CFTS1	0	0	0.111	0	0	0.147	0.045	0.095	
CTTS1	0.127	0.064	0.054	0.064	0.051	0.166	-0.02	-0.016	
WO1	46.629	45.491	2.184	47.349	45.202	1.493	1.703	1.82	
EN1	42.045	42.579	70.314	42.508	43.937	70.032	70.083	70.536	
FS1	10.525	11.083	27.209	9.473	10.139	28.148	28.118	27.552	
Q	2.027	2.007	2.012	1.999	2.022	1.983	1.984	2.006	
J	0.029	0.033	0.005	0.024	0.025	0.002	0.003	0.001	
WO	46.983	45.712	2.338	47.564	45.404	1.796	1.719	1.889	
EN	42.249	42.725	70.01	42.644	44.084	69.623	69.691	70.183	
FS	10.768	11.563	27.652	9.792	10.512	28.581	28.59	27.928	
WEF	98.609	98.378	99.736	98.815	98.776	99.919	99.827	99.963	
Amphibole									
Oxide wt. %	TK-93/1	TK-93/2	TK-93/3	TK-93/4	TK-93/5	TK-93/6	TK-93/7	TK-93/8	TK-93/9
Al2O3	10.145	10.421	10.955	9.722	9.907	10.634	10.4	9.417	10.443
P2O5	-0.026	0.036	0.089	0.043	0.054	-0.028	0.029	-0.026	0.06
K2O	0.089	0.085	0.108	0.114	0.068	0.068	0.111	0.041	0.086
TiO2	0.86	0.719	0.959	0.783	0.809	0.987	0.854	0.606	0.848
Cr2O3	0.491	0.397	0.439	0.46	0.346	0.642	0.467	0.477	0.406
MnO	0.091	0.085	0.128	0.106	0.114	0.178	0.105	0.076	0.132
FeO	9.343	10.02	10.785	9.676	9.336	9.935	10.364	9.835	9.533
CaO	11.174	11.796	11.021	11.882	11.227	12.527	11.314	11.322	10.384
SiO2	49.077	48.581	49.021	48.661	50.704	47.383	48.178	48.964	48.847
Na2O	2.264	2.358	2.344	2.223	2.153	2.305	2.152	2.194	2.322
MgO	15.444	14.911	13.486	15.882	14.226	14.279	15.054	16.152	16.075
NiO	0.046	0.082	0.089	0.129	0.138	0.077	0.044	0.108	0.094
Total	98.998	99.491	99.424	99.681	99.082	99.587	99.072	99.166	99.23
Cations and end members (23 Oxygen)									
TSi	6.455	6.567	6.457	6.608	6.578	6.411	6.612	6.685	6.574
TAl	1.545	1.433	1.543	1.392	1.422	1.589	1.388	1.315	1.426
CAI	0.288	0.46	0.349	0.381	0.418	0.261	0.366	0.333	0.506
CCr	0.059	0.048	0.051	0.056	0.043	0.075	0.053	0.056	0.05
CTi	0.099	0.083	0.106	0.091	0.096	0.11	0.092	0.068	0.1
CMg	3.532	3.336	3.386	3.436	3.345	3.498	3.427	3.58	3.296
CFe2	1.022	1.072	1.108	1.035	1.098	1.056	1.062	0.963	1.048
BFe2	0.254	0.22	0.215	0.218	0.133	0.172	0.179	0.26	0.205
BMn	0.012	0.011	0.016	0.014	0.015	0.022	0.013	0.01	0.018
BCa	1.734	1.769	1.769	1.768	1.851	1.806	1.808	1.731	1.748
ACa	0.152	0.015	0.12	0.038	0.046	0.177	0.081	0.073	0
ANa	0.673	0.705	0.667	0.668	0.658	0.66	0.597	0.632	0.677
AK	0.017	0.017	0.02	0.023	0.014	0.013	0.02	0.008	0.017
Sum_A	0.842	0.737	0.806	0.728	0.718	0.851	0.698	0.713	0.694
Sum_cat	15.842	15.737	15.806	15.728	15.718	15.851	15.698	15.713	15.694
Sum_oxo	22.997	22.997	22.997	22.997	22.997	22.997	22.997	22.997	22.997

Table 3: Representing Electron Probe Microanalysis (EPMA) of pyroxene and feldspar from gabbro

Pyroxene								
Oxide wt. %	TK 93/1	TK 93/2	TK 93/3	TK 93/4	TK 93/5	TK 93/6	TK 93/7	TK 93/8
Al2O3	0.567	0.565	0.307	0.404	0.915	1.514	1.455	1.044
P2O5	-0.004	0.008	0.008	0.004	-0.016	-0.027	0.048	0.004
K2O	-0.006	0.022	-0.021	0.005	0.015	-0.004	-0.004	0.25
TiO2	0.173	0.161	0.186	0.155	0.246	0.333	0.36	0.191
Cr2O3	0.04	0.013	0.02	0.006	0.031	0.026	0.031	0.009
MnO	0.658	0.651	0.629	0.609	0.297	0.338	0.33	0.611
FeO	29.841	31.193	30.824	31.441	15.653	14.921	14.69	29.519
CaO	5.041	2.324	1.005	1.13	20.511	19.832	20.562	4.037
SiO2	49.245	50.462	51.248	49.416	49.138	50.585	51.609	49.908
Na2O	0.018	0.066	0.03	0.027	0.257	0.295	0.215	0.116
MgO	14.208	14.016	15.069	16.053	12.766	11.44	10.626	13.324
NiO	0.06	0.022	0.027	0.041	-0.022	0.004	-0.009	0.049

Total	99.841	99.503	99.332	99.291	99.791	99.257	99.913	99.062
Cations and end members (6 Oxygen)								
TSi	1.934	1.928	1.944	1.954	1.921	1.907	1.896	1.888
TAI	0.028	0.028	0.015	0.02	0.043	0.071	0.068	0.051
MIAI	0	0	0	0	0	0	0	0
MITi	0.005	0.005	0.006	0.005	0.007	0.01	0.011	0.006
M1Fe2	0.112	0.127	0.111	0.13	0.352	0.365	0.358	0.175
M1Cr	0.001	0	0.001	0	0.001	0.001	0.001	0
M1Mg	0.879	0.867	0.881	0.863	0.641	0.624	0.631	0.817
M1Ni	0.002	0.001	0.001	0.001	-0.001	0	0	0.002
M2Mg	0	0	0	0	0	0	0	0
M2Fe2	0.923	0.956	0.972	0.953	0.171	0.135	0.131	0.84
M2Mn	0.023	0.023	0.022	0.021	0.01	0.011	0.011	0.021
M2Ca	0.091	0.059	0.045	0.05	0.834	0.852	0.877	0.178
M2Na	0.001	0.005	0.002	0.002	0.02	0.023	0.017	0.009
M2K	0	0.001	-0.001	0	0.001	0	0	0.013
Sum_cat	4	3.999	4.001	4	3.999	4	4	3.987
Ca	4.474	2.898	2.227	2.472	41.563	42.86	43.68	8.757
Mg	43.332	42.685	43.369	42.781	31.91	31.393	31.408	40.215
Fe2_Mn	52.195	54.418	54.405	54.747	26.527	25.747	24.912	51.028
JD1	0	0	0	0	0	0	0	0
AE1	0.056	0.321	0.066	0.121	1.023	1.137	0.814	1.101
CFTS1	0.009	0	0	0	0	0	0	0
CTTS1	0.269	0.249	0.292	0.24	0.366	0.502	0.535	0.291
WO1	4.245	2.672	1.958	2.255	40.978	42.116	43.03	8.462
EN1	43.807	43.032	43.823	43.184	31.742	31.216	31.326	40.193
FS1	51.614	53.725	53.862	54.2	25.89	25.028	24.294	49.954
Q	2.005	2.009	2.01	1.997	1.997	1.976	1.997	2.01
J	0.003	0.011	0.005	0.004	0.04	0.046	0.033	0.019
WO	4.474	2.898	2.227	2.472	41.563	42.86	43.68	8.757
EN	43.332	42.685	43.369	42.781	31.91	31.393	31.408	40.215
FS	52.195	54.418	54.405	54.747	26.527	25.747	24.912	51.028
WEF	99.857	99.48	99.76	99.787	98.057	97.744	98.374	99.097
Feldspar								
Oxide wt. %	TK-93/1	TK-93/2	TK-93/3	TK-93/4	TK-93/5	TK-93/6		
Al2O3	26.487	27.261	26.949	26.453	26.371	26.709		
P2O5	0.015	0	0.029	-0.02	-0.02	0.055		
K2O	0.343	0.332	0.378	0.303	0.308	0.339		
TiO2	0.014	0.047	0.048	-0.024	0.012	0.005		
Cr2O3	0.031	0	0	-0.008	-0.024	-0.04		
MnO	0.021	-0.014	0.002	-0.02	0.004	0.041		
FeO	0.228	0.23	0.192	0.286	0.284	0.302		
CaO	10.308	11.376	10.862	12.949	12.879	12.077		
SiO2	56.332	54.201	55.522	54.024	55.424	54.204		
Na2O	5.432	5.698	5.475	5.036	4.993	5.678		
MgO	0.017	0.02	0.018	0.022	0.012	0.022		
NiO	-0.018	0.008	-0.071	0.017	-0.037	0.015		
Total	99.21	99.159	99.404	99.018	100.206	99.407		
Cations and end members (32 Oxygen)								
Si	10.159	10.108	10.091	10.002	9.964	10.16		
Al	5.727	5.768	5.761	5.877	5.903	5.675		
Ti	0.002	0.007	0.007	-0.003	0.002	0.001		
Fe2	0.035	0.036	0.03	0.045	0.045	0.047		
Mn	0.003	-0.002	0	-0.003	0.001	0.007		
Mg	0.005	0.006	0.005	0.006	0.003	0.006		
Ca	2.028	2.073	2.073	2.173	2.199	2.024		
Na	1.934	1.916	2.001	1.842	1.84	2.064		
K	0.08	0.079	0.091	0.073	0.075	0.081		
Cations	19.973	19.991	20.059	20.012	20.032	20.065		
X	15.888	15.883	15.859	15.876	15.869	15.836		
Z	4.085	4.108	4.2	4.136	4.163	4.229		
Ab	47.8	47.1	48	45.1	44.7	49.5		
An	50.2	51	49.8	53.2	53.5	48.5		
Or	2	1.9	2.2	1.8	1.8	1.9		

Table 4: Representing Electron Probe Microanalysis of pyroxene, amphibole and feldspar from anorthositic gabbro.

Pyroxene							
Oxide wt. %	TK 86/1	TK 86/2	TK 86/3	TK 86/4	TK 86/5	TK 86/6	
Al ₂ O ₃	0.465	0.584	0.443	1.468	0.117	0.621	
P ₂ O ₅	0.036	0.051	0.02	0.012	-0.023	0.028	
K ₂ O	0.01	0.017	0.046	0.069	-0.029	-0.018	
TiO ₂	0.057	0.053	0.087	0.143	0.036	0.136	
Cr ₂ O ₃	-0.009	0.022	-0.004	0.011	0.001	0.022	
MnO	0.273	0.867	0.33	0.296	0.49	0.768	
FeO	26.708	29.549	28.078	23.293	19.641	27.797	
CaO	13.213	9.293	11.212	13.956	23.042	9.586	
SiO ₂	50.234	51.267	50.678	52.562	49.225	53.235	
Na ₂ O	0.067	0.155	0.137	0.155	0.055	0.118	
MgO	8.032	7.598	8.626	7.875	6.531	7.607	
NiO	0.004	0	-0.039	0.039	-0.016	-0.027	
Total	99.09	99.456	99.614	99.879	99.07	99.873	
Cations and end members (6 Oxygen)							
TSi	2.083	2.053	2.044	2.016	1.926	2.038	
TAI	0	0	0	0	0.006	0	
M1Al	0.023	0.029	0.022	0.074	0	0.032	
M1Ti	0.002	0.002	0.003	0.005	0.001	0.004	
M1Fe ₂	0.475	0.485	0.432	0.42	0.601	0.475	
M1Cr	0	0.001	0	0	0	0.001	
M1Mg	0.501	0.483	0.545	0.5	0.399	0.489	
M1Ni	0	0	-0.001	0.001	-0.001	-0.001	
M2Mg	0	0	0	0	0	0	
M2Fe ₂	0.354	0.569	0.421	0.411	0.038	0.528	
M2Mn	0.01	0.031	0.012	0.011	0.017	0.028	
M2Ca	0.547	0.333	0.509	0.546	1.011	0.397	
M2Na	0.005	0.013	0.011	0.013	0.004	0.01	
M2K	0.001	0.001	0.002	0.004	-0.002	-0.001	
Sum_cat	3.999	3.999	3.998	3.996	4.002	4.001	
Ca	29.003	17.525	26.525	28.929	48.956	20.702	
Mg	26.539	25.404	28.395	26.512	19.307	25.52	
Fe ₂ _Mn	44.458	57.071	45.08	44.558	31.737	53.778	
JD1	0.317	0.729	0.715	0.875	0	0.468	
AE1	0	0	0	0	0.139	0	
CFTS1	0	0.039	0	0.02	0	0.039	
CTTS1	0	0	0	0	0.054	0	
WO1	29.06	17.649	26.499	28.82	49.24	20.872	
EN1	26.592	25.641	28.367	26.43	19.44	25.778	
FS1	44.032	55.941	44.419	43.856	31.127	52.843	
Q	1.876	1.87	1.907	1.877	2.048	1.889	
J	0.011	0.026	0.023	0.026	0.009	0.02	
WO	29.003	17.525	26.525	28.929	48.956	20.702	
EN	26.539	25.404	28.395	26.512	19.307	25.52	
FS	44.458	57.071	45.08	44.558	31.737	53.778	
WEF	99.427	98.67	98.84	98.661	99.579	98.981	
Amphibole							
Oxide wt. %	TK-86/1	TK-86/2	TK-86/3	TK-86/4	TK-86/5	TK-86/6	TK-86/7
Al ₂ O ₃	8.284	7.655	7.396	6.731	5.784	8.071	8.351
P ₂ O ₅	0.024	0.008	0.055	-0.039	0.004	0	0.012
K ₂ O	1.156	1.027	1.006	0.729	0.462	1.098	1.201
TiO ₂	1.837	1.546	1.453	0.299	0.099	1.519	2.021
Cr ₂ O ₃	0.003	-0.009	-0.004	-0.019	0.017	-0.003	-0.037
MnO	0.298	0.262	0.318	0.363	0.446	0.313	0.27
FeO	24.257	25.275	26.732	24.77	25.904	23.577	23.514
CaO	10.752	10.947	10.92	11.735	10.624	10.268	10.196
SiO ₂	46.23	45.945	45.536	47.587	48.934	48.167	47.445
Na ₂ O	1.133	1.06	0.963	0.923	0.705	1.148	0.917
MgO	5.111	5.287	4.852	6.047	6.06	5.252	5.299
NiO	-0.005	0.026	0.017	-0.048	-0.022	-0.026	-0.06
Total	99.08	99.029	99.244	99.078	99.017	99.384	99.129
Cations and end members (23 Oxygen)							
TSi	6.616	6.674	6.659	6.931	7.146	6.569	6.526
TAI	1.384	1.326	1.341	1.069	0.854	1.431	1.474
CAI	0.219	0.17	0.103	0.242	0.256	0.168	0.162

CCr	0	-0.001	-0.001	-0.002	0.002	0	-0.005	
CTi	0.227	0.193	0.181	0.037	0.012	0.192	0.253	
CMg	1.252	1.307	1.199	1.492	1.473	1.317	1.313	
CFe2	3.301	3.331	3.517	3.231	3.256	3.323	3.277	
BFe2	0.116	0.175	0.19	0.196	0.207	0.164	0.131	
BMn	0.041	0.037	0.045	0.051	0.062	0.045	0.038	
BCa	1.843	1.788	1.765	1.753	1.731	1.791	1.831	
ACa	0.051	0.104	0.175	0.15	0.124	0.132	0.128	
ANa	0.361	0.341	0.31	0.296	0.223	0.375	0.296	
AK	0.242	0.217	0.213	0.154	0.096	0.236	0.255	
Sum_A	0.654	0.662	0.697	0.6	0.443	0.742	0.678	
Sum_cat	15.654	15.662	15.697	15.6	15.443	15.742	15.678	
Sum_oxo	22.998	22.998	22.998	22.998	22.998	22.998	22.998	
Feldspar								
Oxide wt. %	TK-86/1	TK-86/2	TK-86/3	TK-86/4	TK-86/5	TK-86/6	TK-86/7	TK-86/8
Al ₂ O ₃	25.876	24.901	24.97	24.698	25.176	24.063	20.384	21.932
P ₂ O ₅	0.063	-0.016	0.004	-0.023	-0.008	0.021	-0.009	0.026
K ₂ O	0.23	0.373	0.591	0.534	0.367	0.378	0.111	0.074
TiO ₂	0.084	0.04	0.051	0.106	0.06	0.035	0.048	-0.016
Cr ₂ O ₃	0.034	-0.058	0.012	0.001	0.003	0.035	0.033	-0.018
MnO	-0.011	-0.002	-0.026	-0.008	-0.027	-0.007	-0.012	0.02
FeO	0.255	0.249	0.306	0.231	0.235	0.217	0.23	0.052
CaO	8.531	10.182	9.356	9.126	11.115	10.181	1.728	0.544
SiO ₂	57.428	56.965	58.159	57.951	57.016	58.19	63.354	63.933
Na ₂ O	6.989	6.445	6.68	6.485	6.5	7.246	13.456	12.964
MgO	0.002	0.01	0.01	-0.01	0.008	0.025	0.029	0.006
NiO	-0.055	0.045	0.03	0.012	0.008	-0.063	0	0.026
Total	99.426	99.134	100.143	99.103	100.453	100.321	99.352	99.543
Cations and end members (32 Oxygen)								
Si	10.487	10.378	10.506	10.532	10.442	10.43	11.696	11.94
Al	5.35	5.438	5.267	5.36	5.451	5.454	4.214	4.01
Ti	0.012	0.006	0.007	0.015	0.009	0.005	0.007	-0.002
Fe ₂	0.039	0.039	0.046	0.036	0.037	0.035	0.036	0.008
Mn	-0.002	0	-0.004	-0.001	-0.004	-0.001	-0.002	0.003
Mg	0.001	0.003	0.003	-0.003	0.002	0.007	0.008	0.002
Ca	1.669	1.824	1.795	1.604	1.644	1.687	0.342	0.11
Na	2.475	2.317	2.32	2.317	2.383	2.331	3.743	3.941
K	0.054	0.088	0.135	0.126	0.089	0.093	0.026	0.018
Cations	20.085	20.093	20.075	19.986	20.053	20.041	20.07	20.03
X	15.849	15.822	15.78	15.907	15.902	15.889	15.917	15.948
Z	4.236	4.271	4.295	4.079	4.151	4.152	4.153	4.082
Ab	59	54.8	54.6	57.3	57.9	56.7	91	96.9
An	39.8	43.1	42.2	39.6	39.9	41	8.3	2.7
Or	1.3	2.1	3.2	3.1	2.2	2.3	0.6	0.4

Table 5: Chemical results of major elements (wt. %) and trace elements (ppm) of peridotite belonging to Intrusive Unit, Singhbhum Craton, Eastern India

Sample no.	T-110	T-85	T-86	T-88	T- 150	T- 156	TK-583	TK-586
Rock name	Peridotite							
SiO ₂	41.32	44.32	41.44	42.97	39.58	39.29	45.04	43.05
Al ₂ O ₃	3.3	3.28	3.38	3.62	3.39	3.15	4.44	4.49
Fe ₂ O ₃ (t)	8.5	12.45	9.68	9.25	9.47	10.43	10.88	11.34
MnO	0.13	0.17	0.14	0.13	0.13	0.17	0.16	0.18
MgO	33.53	27.67	31.55	31.47	34.71	35.25	27.87	27.41
CaO	3.51	6.41	5.23	4.53	3.55	2.44	5.22	7.07
Na ₂ O	0.14	0.34	0.2	0.32	0.14	0.06	0.47	0.3
K ₂ O	0.08	0.06	0.05	0.09	0.04	0.04	0.08	0.07
TiO ₂	0.28	0.47	0.29	0.28	0.25	0.25	0.44	0.33
P ₂ O ₅	0.01	0.1	0.01	0.1	0	0.02	0	0
LOI	8.32	4.05	7.2	6.54	7.87	7.46	4.59	4.97
Ba	50	40	25	45	50	35	45	40
Cu	20	55	265	90	20	10	55	70
Pb	5	5	5	5	5	5	5	5
Zn	25	40	90	65	25	110	40	45
Ni	1700	1330	130	265	1700	1680	1330	1035
Co	45	100	55	66	78	45	100	80
Cr	2995	2845	425	1115	2995	8240	2845	2840

Nb	1.5	2	1.5	3	1.9	2	3	2
Rb	10	10	5	5	10	5	10	5
Y	10	15	20	25	10	10	15	15
V	123	135	260	145	175	143	135	140
Zr	20	40	30	75	20	45	40	25
Sr	15	60	125	140	15	15	60	60
Ga	10	10	15	15	10	15	10	10
Sc	13	18	40	24	28	18	25	25
La	1.75	3.45	1.25	1.83	1.30	3.70	3.34	2.59
Ce	3.29	6.69	2.32	3.45	2.48	7.94	6.29	5.30
Pr	0.5	0.97	0.5	0.5	0.5	0.90	0.82	0.76
Nd	1.62	3.68	1.23	1.70	1.15	3.16	2.74	2.46
Eu	1.25	1.05	1.62	1.53	0.94	1.45	0.56	1.45
Sm	0.52	0.94	0.5	0.5	0.84	1.25	0.71	0.72
Gd	0.67	1.37	0.65	0.63	0.59	0.92	1.08	1.23
Tb	0.5	0.5	0.5	0.5	0.5	0.5	0.5	0.5
Dy	0.87	1.48	0.99	0.82	0.84	1.06	1.30	1.58
Ho	0.5	0.5	0.5	0.5	0.5	0.5	0.5	0.5
Er	0.53	0.86	0.66	0.54	0.52	0.64	0.80	0.89
Tm	0.5	0.5	0.5	0.5	0.5	0.5	0.5	0.5
Yb	0.57	0.86	0.70	0.55	0.57	0.64	0.84	0.94
Lu	0.5	0.5	0.5	0.5	0.5	0.5	0.5	0.5
ΣREE	13.57	23.35	12.42	14.05	11.73	23.66	20.48	19.92
ΣLREE	8.93	16.78	7.42	9.51	7.21	18.40	14.46	13.28
ΣHREE	4.64	6.57	5.00	4.54	4.52	5.26	6.02	6.64
(La/Yb)N	2.07	2.70	1.20	2.24	1.54	3.90	2.68	1.86
(La/Sm)N	2.12	2.31	1.57	2.30	0.97	1.86	2.96	2.26
(Gd/Yb)N	0.95	1.29	0.75	0.92	0.84	1.16	1.04	1.06
(Sm/Nd)N	0.99	0.79	1.25	0.90	2.24	1.22	0.80	0.90
Eu/Eu*	6.48	2.83	8.69	8.34	4.08	4.13	1.96	4.71
Ce/Ce*	0.87	0.87	0.85	0.88	0.89	1.01	0.89	0.95
Fe2O3/(Fe2O3 + MgO)	0.20	0.31	0.23	0.23	0.21	0.23	0.28	0.29
Al2O3/ TiO2	11.79	6.98	11.66	12.93	13.56	12.60	10.09	13.61
CaO/Al2O3	1.06	1.95	1.55	1.25	1.05	0.77	1.18	1.57
Na2O+K2O	0.22	0.40	0.25	0.41	0.18	0.10	0.55	0.37
Nb/Y	0.15	0.16	0.08	0.10	0.19	0.20	0.18	0.13
Nb/La	0.86	0.70	0.82	0.67	0.73	0.54	0.81	0.77
Nb/Yb	2.63	2.79	2.14	4.55	3.33	3.13	3.21	2.13
Ce/Yb	5.77	7.78	3.31	6.27	4.35	12.41	7.49	5.64
Zr/Y	2.00	2.67	1.50	3.00	2.00	4.50	2.67	1.67
Zr/Yb	35.09	46.51	42.86	136.36	35.09	70.31	47.62	26.60
Ba/Zr	2.50	1.00	0.83	0.60	2.50	0.78	1.13	1.60
La/Yb	3.07	4.01	1.79	3.33	2.28	5.78	3.98	2.76
La/Nb	1.17	1.44	0.83	0.73	0.68	1.85	1.24	1.30

Table 6: Chemical results of major elements (wt. %) and trace elements (ppm) of gabbro and anorthositic gabbro belonging to Intrusive Unit, Singhbhum Craton, Eastern India.

Sample no.	TK-243	TK-244	TK-335	TK-487	TK-486	T-64	T-61	T-60	TK-86	TK-581	TK-582	TK-587	TK-588
Rock name	Gabbro								Anorthositic gabbro				
SiO2	51.7	51.49	53.22	52.28	50.82	53.84	50.43	50.28	54.62	52.44	57.44	55.54	50.85
Al2O3	10.39	11.62	15.74	12.34	11.76	13.53	11.81	12.19	16.46	14.03	15.34	22.63	15.64
Fe2O3 (t)	15.46	15.2	11.58	13.47	13.85	11.41	16.76	16.57	12.78	14.79	8.67	4.83	14.45
MnO	0.16	0.14	0.17	0.15	0.16	0.17	0.17	0.17	0.12	0.15	0.04	0.06	0.14
MgO	6.61	6.02	4.85	6.23	7.66	7.17	5.55	5.63	1.71	3.02	3.56	1.02	2.16
CaO	8.24	8.04	7.15	8.05	8.54	8.85	7.01	6.66	7.54	8.34	6.34	8.61	8.16
Na2O	2.63	2.79	3.79	2.55	2.54	1.76	2.93	2.89	3.25	3.32	4.04	4.64	3.58
K2O	0.67	0.69	1.02	1.11	0.66	0.42	1.14	1.24	0.75	0.7	1.11	0.67	0.53
TiO2	1.96	1.97	0.32	1.51	1.48	0.32	1.71	1.79	1.02	1.6	1.34	0.28	1.31
P2O5	0.18	0.15	0.05	0.19	0.14	0.08	0.25	0.35	0.12	0.15	0.04	0.27	0.29
LOI	1.48	1.37	1.68	1.69	1.95	1.97	1.61	1.72	1.14	0.97	0.87	0.89	2.34
Ba	145	169	218	265	165	210	170	200	210	280	420	255	310
Cu	135	140	55	110	190	220	375	410	45	125	15	30	330
Pb	5	10	15	10	10	10	5	5	10	15	25	10	5
Zn	95	100	90	85	110	95	155	140	90	110	40	45	110
Ni	100	110	75	120	165	130	170	185	28	55	15	15	30
Co	54	65	48	55	60	65	60	65	16	55	5	20	55
Cr	65	50	15	65	160	35	200	215	28	70	15	20	35

Nb	10	5	5	10	10	5	10	10	5	10	5	2.5	5
Rb	20	20	40	35	30	15	25	45	20	25	10	20	15
Y	25	20	20	25	20	20	25	25	20	15	15	15	15
V	257	213	169	320	325	175	250	235	160	150	30	20	380
Zr	145	115	45	165	145	75	200	195	35	50	250	35	75
Sr	250	280	210	225	210	225	495	420	420	345	295	530	390
Ga	20	20	25	20	20	15	20	16	20	20	15	20	25
Sc	20	22	18	25	30	28	20	45	25	50	5	20	30
La	26.31	21.43	8.87	25.23	20.91	12.95	38.69	38.07	13.25	11.95	26.66	10.92	16.54
Ce	51.14	41.32	16.27	47.79	41.38	23.76	72.76	72.28	24.67	22.19	50.94	20.74	30.97
Pr	6.74	5.37	1.99	6.33	5.30	2.81	9.59	9.32	3.15	2.85	5.08	2.49	3.79
Nd	24.91	18.99	7.04	23.17	18.57	10.47	34.83	34.59	10.14	9.64	17.67	8.49	12.82
Eu	1.43	1.48	0.81	1.25	1.06	0.55	1.67	1.56	0.65	0.56	0.80	0.5	0.63
Sm	5.40	4.79	2.02	4.65	3.98	2.06	7.06	6.69	2.43	2.09	3.63	1.74	2.76
Gd	6.06	5.04	2.04	5.59	4.81	2.42	8.32	8.18	2.78	2.53	2.32	1.85	3.01
Tb	0.90	0.76	0.5	0.83	0.74	0.5	1.20	1.16	0.5	0.5	0.5	0.5	0.5
Dy	4.96	4.07	2.12	4.45	3.89	2.33	6.66	6.45	2.68	2.20	1.17	1.38	2.39
Ho	0.89	0.73	0.5	0.82	0.72	0.5	1.16	1.10	0.51	0.5	0.5	0.5	0.5
Er	2.43	1.97	1.27	2.27	1.95	1.31	3.19	3.03	1.54	1.10	0.72	0.72	1.25
Tm	0.5	0.5	0.5	0.5	0.5	0.5	0.5	0.5	0.5	0.5	0.5	0.5	0.5
Yb	2.12	1.80	1.35	2.08	1.76	1.40	2.82	2.66	1.71	1.23	0.89	0.69	1.19
Lu	0.5	0.5	0.5	0.5	0.5	0.5	0.5	0.5	0.5	0.5	0.5	0.5	0.5
ΣREE	134.29	108.75	45.78	125.46	106.07	62.06	188.95	186.09	65.01	58.34	111.88	51.52	77.35
ΣLREE	115.93	93.38	37.00	108.42	91.20	52.60	164.60	162.51	54.29	49.28	104.78	44.88	67.51
ΣHREE	18.36	15.37	8.78	17.04	14.87	9.46	24.35	23.58	10.72	9.06	7.10	6.64	9.84
(La/Yb)N	8.37	8.03	4.43	8.18	8.01	6.24	9.25	9.65	5.22	6.55	20.20	10.67	9.37
(La/Sm)N	3.06	2.81	2.76	3.41	3.30	3.95	3.45	3.58	3.43	3.60	4.62	3.95	3.77
(Gd/Yb)N	2.31	2.26	1.22	2.17	2.21	1.39	2.38	2.48	1.31	1.66	2.10	2.16	2.04
(Sm/Nd)N	0.67	0.78	0.88	0.62	0.66	0.61	0.62	0.60	0.74	0.67	0.63	0.63	0.66
Eu/Eu*	0.76	0.92	1.22	0.75	0.74	0.75	0.67	0.64	0.76	0.74	0.84	0.85	0.67
Ce/Ce*	0.90	0.90	0.88	0.88	0.93	0.87	0.88	0.88	0.89	0.88	0.94	0.91	0.90
Fe ₂ O ₃ / (Fe ₂ O ₃ + MgO)	0.70	0.72	0.70	0.68	0.64	0.61	0.75	0.75	0.88	0.83	0.71	0.83	0.87
Al ₂ O ₃ / TiO ₂	5.30	5.90	49.19	8.17	7.95	42.28	6.91	6.81	16.14	8.77	11.45	80.82	11.94
CaO/Al ₂ O ₃	0.79	0.69	0.45	0.65	0.73	0.65	0.59	0.55	0.46	0.59	0.41	0.38	0.52
Na ₂ O+K ₂ O	3.30	3.48	4.81	3.66	3.20	2.18	4.07	4.13	4.00	4.02	5.15	5.31	4.11
Nb/Y	0.40	0.25	0.25	0.40	0.50	0.25	0.40	0.40	0.25	0.67	0.33	0.17	0.33
Nb/La	0.38	0.23	0.56	0.40	0.48	0.39	0.26	0.26	0.38	0.84	0.19	0.23	0.30
Nb/Yb	4.72	2.78	3.70	4.81	5.68	3.57	3.55	3.76	2.92	8.13	5.62	3.62	4.20
Ce/Yb	24.12	22.96	12.05	22.98	23.51	16.97	25.80	27.17	14.43	18.04	57.24	30.06	26.03
Zr/Y	5.80	5.75	2.25	6.60	7.25	3.75	8.00	7.80	1.75	3.33	16.67	2.33	5.00
Zr/Yb	68.40	63.89	33.33	79.33	82.39	53.57	70.92	73.31	20.47	40.65	280.90	50.72	63.03
Ba/Zr	1.00	1.47	4.84	1.61	1.14	2.80	0.85	1.03	6.00	5.60	1.68	7.29	4.13
La/Yb	12.41	11.91	6.57	12.13	11.88	9.25	13.72	14.31	7.75	9.72	29.96	15.83	13.90
La/Nb	2.63	4.29	1.77	2.52	2.09	2.59	3.87	3.81	2.65	1.20	5.33	4.37	3.31